Molecular Determinants of Optical Modulation in ssDNA-Carbon Nanotube Biosensors: Insights from Experimental and Computational Approaches

Andrew T. Krasley[1, †], Sayantani Chakraborty[2, †], Lela Vuković[2,3,*], Abraham G. Beyene[1,*]

[1] Janelia Research Campus, Howard Hughes Medical Institute, Ashburn, VA 20147

[2] Department of Chemistry and Biochemistry, University of Texas at El Paso, El Paso, TX 79968

[3] Computational Science Program and Bioinformatics Program, University of Texas at El Paso, El Paso, TX 79968

* Corresponding authors. Email: lvukovic@utep.edu; beyenea@janelia.hhmi.org

† These authors contributed equally to this work.

Abstract

Most traditional optical biosensors operate through molecular recognition, where ligand binding causes conformational changes that lead to optical perturbations in the emitting motif. Optical sensors developed from single-strand DNA functionalized single-walled carbon nanotubes (ssDNA-SWCNT) have started to make useful contributions to biological research. However, the mechanisms underlying their function have remained poorly understood. In this study, we used a combination of experimental and computational approaches to show that ligand binding alone is not sufficient for optical modulation in this class of synthetic biosensors. Instead, the optical response that occurs after ligand binding is highly dependent on the chemical properties of the ligands, resembling mechanisms seen in activity-based biosensors. Specifically, we show that in ssDNA-SWCNT catecholamine sensors, the optical response correlates positively with electron density on the aryl motif, even when ligand binding affinities are similar. These findings could serve as a foundation for tuning the performance of existing sensors and guiding the development of new biosensors of this class.

Introduction

The photoluminescence properties of single-walled carbon nanotubes (SWCNTs), which originate from quantum confined surface excitons, have been exploited for a variety of biological applications, including fluorescence imaging[1], single-particle tracking[2-5], and biosensing[1,6,7]. These applications take advantage of the nanotube's unique photophysical traits, such as photoluminescence in the near-infrared and shortwave infrared regions of the spectrum, as well as their non-blinking and photostable emission. In biosensing, the excitonic fluorescence of SWCNTs and their distinctive single-atom-thick geometry are exploited to translate molecular recognition events into detectable signals. The optoelectronic properties of SWCNT, and similar shell-like nanomaterials, are highly sensitive to physicochemical perturbations that occur on or near the surface, enabling detection of local changes with single-molecule sensitivity. This has been successfully demonstrated in functionalized SWCNTs.[8-10]

Biosensing applications of SWCNTs require functionalization with moieties that tailor the pristine surface of the nanomaterials, creating configurations ideal for analyte binding. Among the various strategies for developing SWCNT-based biosensors, noncovalent functionalization with amphiphilic biopolymers, particularly oligonucleotides (e.g., single-strand DNA, ssDNA) remains a predominant strategy.[1,11-16] This approach enables versatile patterning of the nanotube surface with chemically rich and structurally diverse oligonucleotide motifs. This strategy has enabled successful applications of ssDNA-SWCNT hybrids in diverse fields, including nanotube-based device manufacturing[17,18], chirality sorting[19,20], and SWCNT lattice remodeling[21]. The conjugation of ssDNA to the surface of nanotubes through noncovalent self-assembly sculpts specific analyte binding pockets that are absent on non-functionalized surfaces, enabling their use in biosensing applications.[1,11-16]

Despite several successful applications, a coherent strategy for developing biosensors from ssDNA-SWCNT bio-nanohybrids remains elusive. This challenge stems in part from a lack of understanding of how analyte binding in ssDNA-nanotube bio-nano conjugates modulates the optical properties of the nanotubes. The chemical diversity of nanotube surface topologies that can be engineered with ssDNA sequences is vast and depends on oligonucleotide length and sequence chemistry. Matching this broad chemical space to potential analytes through screening approaches is an arduous task, and success with this approach has been limited.[11,22,23] Recent studies have demonstrated that machine learning approaches hold promise for predicting new ssDNA sequences in ssDNA-SWCNTs for sensing small molecular analytes.[24-26] An alternative approach is rational design, where mechanistic understanding of how ssDNA-SWCNT biosensors function guides sensor development. Such understanding could streamline the development of biosensors by informing the selection or chemical modification of ssDNA sequences and the design of nanotube functionalization strategies, ultimately leading to more effective and predictable sensor development and performance.

To better understand mechanisms of fluorescence modulation in ssDNA-SWCNT, we performed a structure-activity relationship study on a class of sensors for catechol (benzene-1,2-diol)-bearing small molecules. Previous studies have shown that $(GT)_N$-SWCNT (N = 6-15) conjugates undergo a strong fluorescence turn-on in response to catecholamines, with reported affinities in the nanomolar to single micromolar range.[11,27,28] These sensors have enabled significant advancement in the field of catecholamine biology, including dopamine (4-(2-aminoethyl) benzene-1,2-diol), in cell cultures[28-30] and tissues[27]. Nanotube-based catecholamine sensors are notable for their robustness, intensiometric readout, high signal-to-noise ratio, and rapid, and reversible responses – attributes highly valued in biological applications. We propose that this class of sensors can serve as a model system from which mechanistic insights benefitting the broader field may emerge. By focusing on these well-characterized systems, we aim to elucidate the fundamental principles governing the interaction between ssDNA functionalized SWCNTs and their analytes, potentially paving the way for the rational design of new biosensors.

In pursuit of this goal, we combined experimental and computational approaches to better understand how compounds bearing the catechol-motif modulate the fluorescence of $(GT)_6$-SWCNT conjugates. Experimentally, we observed that optical modulation in these sensors is strongly influenced by certain electrochemical properties of catechols. Manipulating electron densities on the aryl motif of catechols sensitively alters fluorescence turn-on response, with higher electron densities correlating positively with stronger turn-on response. Reduction potentials also reflected this trend, where electron-rich catechol oxidized more easily and elicited stronger fluorescence turn-on responses. Interestingly however, no oxidative products were generated during the molecular recognition process, as implied by the correlation between optical response and reduction potential. This suggested that a transient perturbative phenomenon, rather than permanent charge transfer, is responsible for optical modulation observed in these sensors. To rationalize our experimental observations, we employed molecular dynamics (MD)

2

88 simulations. These simulations provided insights into analyte-sensor interactions, which, when combined
89 with experimental data, allowed us to identify key molecular parameters that collectively define a
90 "perturbation cross section" for catechol-bearing ligands. Our work suggests that ligand binding and
91 analyte electrochemical properties play a concerted role in modulating optical responses in ssDNA-
92 SWCNT biosensors.
93
94 **Results**
95
96 To investigate optical responses in $(GT)_6$-SWCNT conjugates, we generated a library of small molecules,
97 using dopamine as our principal compound. The library was designed with variations in truncation,
98 extension, and substitution patterns around the aryl group. The library included conjugated and
99 unconjugated systems, as well as aryl groups with bulky substituents to assess steric effects. Electron-
100 donating and -withdrawing substituents, along with hydrogen bond donors and acceptors, were installed at
101 various positions to explore electronic effects and binding interactions (Fig. 1). We measured the
102 fluorescence modulation caused by each analyte in solution phase experiments by recording emission
103 intensity before and after addition of 10 µM of each analyte and reported the relative change in intensity
104 from integrated spectra (ΔF/F) (fig. S1). To enable comparison across replicates, we normalized the
105 responses to the modulation measured for dopamine under the same experimental conditions. The
106 screening results showed that the majority of the screened analytes produced no optical responses (Fig. 1c
107 IV, 53%). The responses generated by the remaining analytes varied widely, and included optical
108 modulations that are stronger than that produced by dopamine (Fig. 1c I, 15%), comparable with
109 dopamine (Fig. 1c II, 6%), and weaker than dopamine (Fig. 1c III, 26%).
110
111 Closer examination of the screening results reveals a key requirement to elicit optical response: *ortho*
112 hydrogen bond donors installed on π-conjugated scaffolds. Non-catechols can be tolerated if they satisfy
113 these two criteria (e.g., **RR**, **O**). Changing the position of the hydrogen bond donors from *ortho* (**T**) to
114 *meta* (**1**) leads to loss of optical response. Interestingly, compound **4** elicited a response, even though the
115 hydroxyls are closer than the van der Walls radii on *ortho*-substituted aryls. This suggests that conjugated
116 systems with hydrogen bond donors less than ~3.1 Å[31] apart could be effective sensor substrates. Loss in
117 response also occurs if the hydrogen bond donors are unconjugated (e.g., **BB**, **G**) or replaced with an
118 acceptor (e.g., **FF**, **6**, **GG**, **H**, **P**, **Q**). Sterically bulky compounds meeting these criteria were well
119 tolerated in producing responses (e.g., **4**, **TT**, **UU**, **W**). This suggests that the binding pocket of
120 interactions is likely to be shallow or is at least very accessible.
121
122 As expected, most optical modulations were generated by compounds bearing the catechol motif, whereas
123 other molecules generated modest or no responses. Interestingly, the catechol motif was not a guarantee
124 of the presence of a fluorescence modulation, and even within the catechol family of molecules, optical
125 responses varied widely (Fig. 2). This observation suggested that the heuristics described earlier are useful
126 qualitative descriptors, but they do not fully capture the trends in optical responses. We therefore set out
127 to identify molecular properties that could offer better quantitative explanation of the observed variability
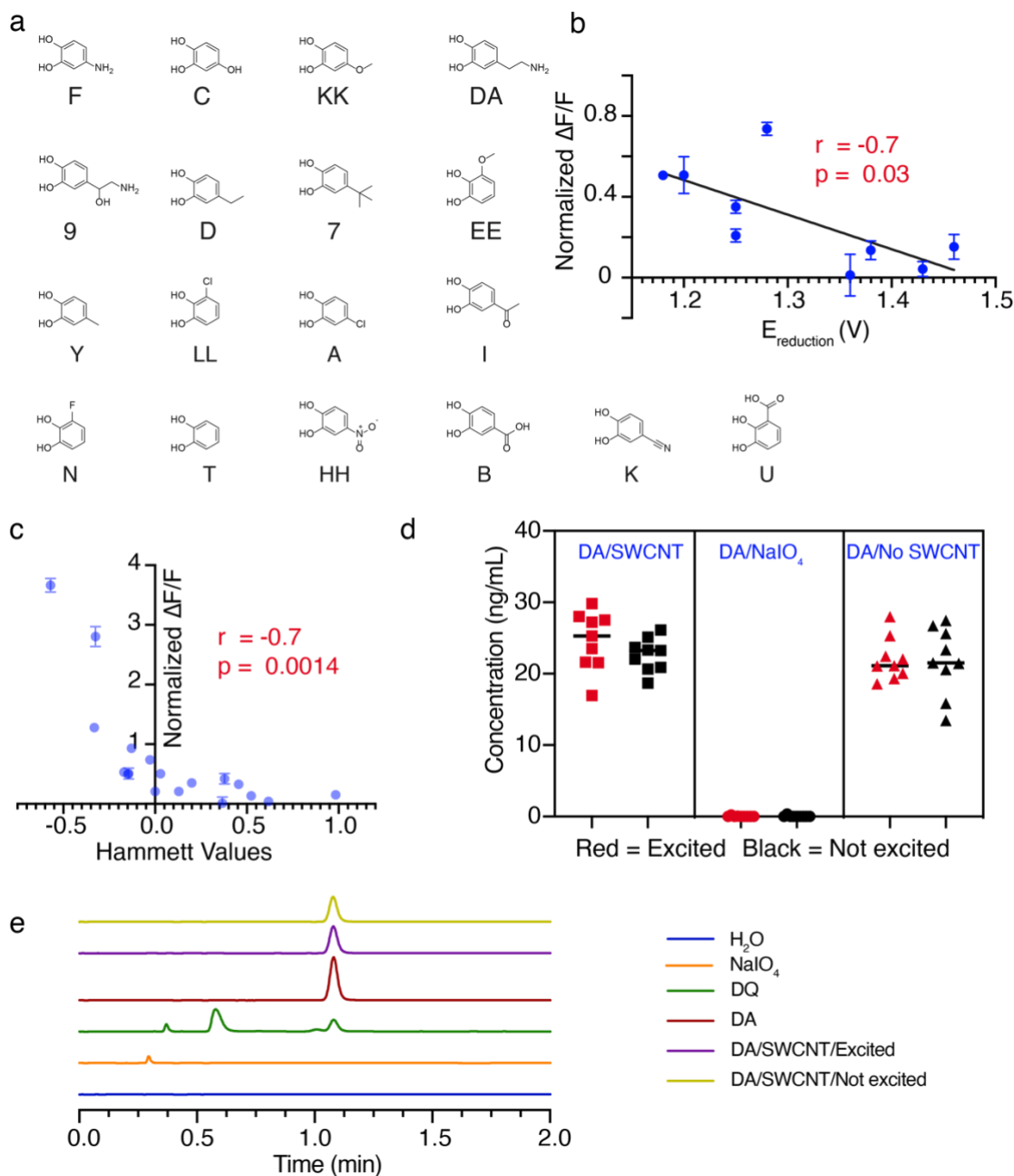128 in optical responses.
129
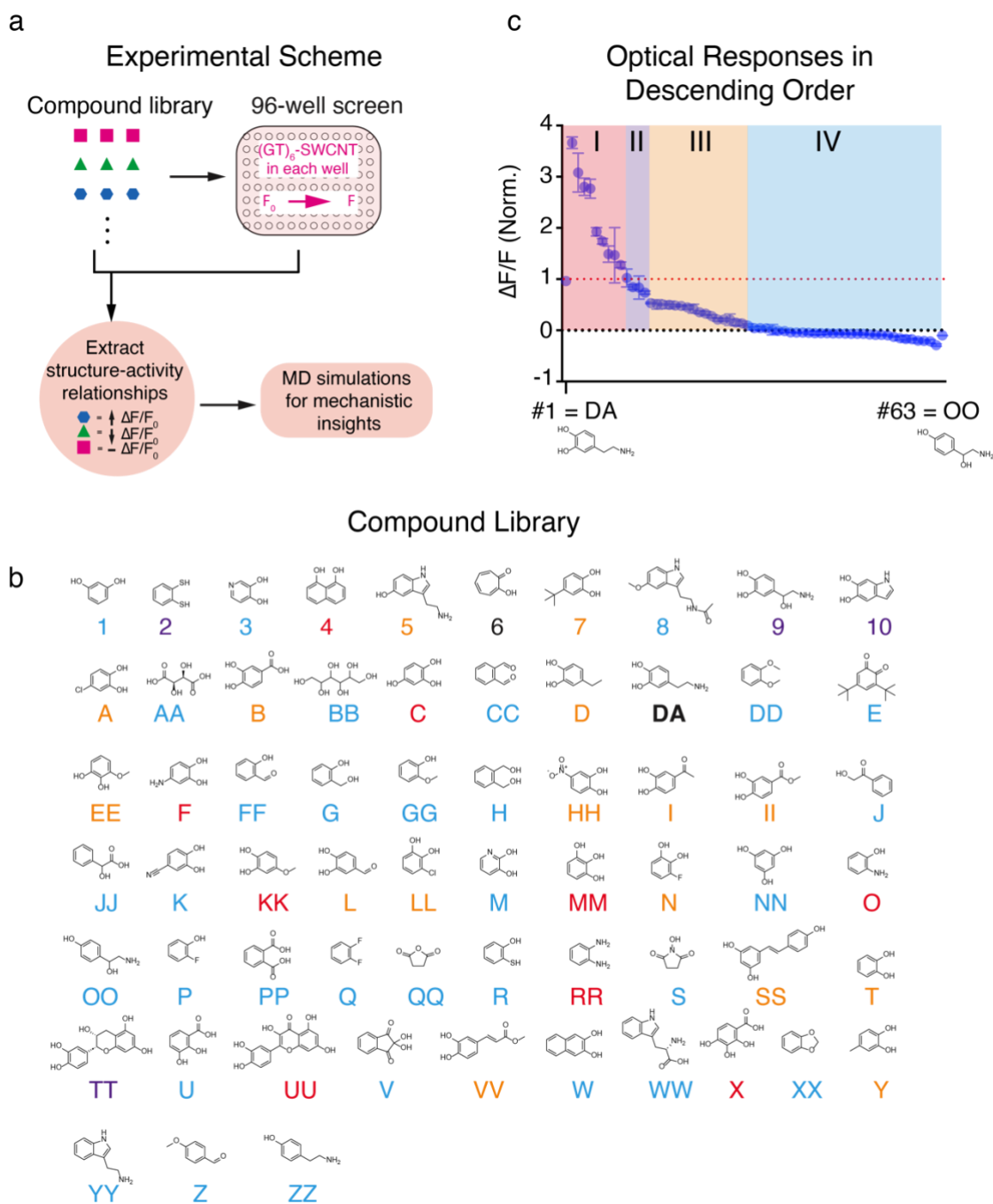
Fig. 1. Experimental schematic and screening library. a, study workflow. **b,** library of the 63 compounds screened; labels are color coded to match optical response categories shown in (**c**). **c,** Normalized (mean) fluorescence responses (normalized to dopamine = 1.00) in descending order. Group I analytes have high responses (≥ 1.00), group II have intermediate responses ($0.75 - 1.00$). group III have low responses ($0.15 - 0.50$), and group IV elicit no response (< 0.10). See Table S1 for a full list of $\Delta F/F$ mean values and standard deviations.

Towards this goal, we explored molecular correlates of optical modulation by assessing if certain physicochemical parameters of these molecules correlated with optical responses. To facilitate comparison and minimize contributions that might arise from significant differences in molecular structure and steric effects, we selected a subset of 18 compounds, each bearing a catechol motif with simple substituents at different positions on the aryl ring (Fig. 2a). We then investigated correlation

4

between 12 different cheminformatic parameters of these molecules and the optical modulations generated by each. These properties included the strength of dipole moment, polarizability, LogP, and van der Waals surface area, among others. The analysis demonstrated a general lack of correlation between the experimentally measured optical responses and all 12 of the physicochemical attributes examined (Fig. S2 and S3).

Fig. 2. Molecular correlates of optical response. **a,** Subset of 18 compounds from 63 screened used for comparative analysis. **b,** Normalized fluorescence responses (mean, DA = 1.00) vs. reduction potentials from Pelizzetti et al.[32] for 9 compounds. Compounds that more readily underwent oxidation produced larger changes in fluorescence. See Table S2 for ΔF/F values and reduction potentials. **c,** Normalized fluorescence response (mean, DA = 1.00) vs. Hammett values for the 18-compound subset demonstrating that more electron donating substituents produced larger changes in fluorescence. See Table S3 for ΔF/F and Hammett values. **d,** Dopamine ELISA assay showing no difference in amounts of dopamine between those samples exposed to 658 nm light (104.8 mW, 60 min, Excited) and those that were unexposed (Not excited). As a control, dopamine was oxidized to dopaquinone (DQ) with $NaIO_4$ to demonstrate that dopamine depletion (by oxidation to quinone) can be detected as a loss of

5

157 signal by the assay (DA/NaIO$_4$). As another control, dopamine in 0.1M NaCl without SWCNT in solution were exposed to
158 laser to show no oxidation occurs (DA/No SWCNT). See fig. S7 for more details about assay. **e,** High-performance liquid
159 chromatography (HPLC) analysis of exposed (658 nm, 105.8 mW, 60 min, Excited) and unexposed (Not excited) samples
160 along with controls showing only dopamine was detected in both samples with no detection of dopaquinone or any other
161 oxidized products (Blue: H$_2$O, Orange: NaIO$_4$, Green: dopaquinone (dopamine oxidized with substoichiometric amount of
162 NaIO$_4$), Red: dopamine, Purple: 20 ppm SWCNT + 10 µM dopamine exposed to 658 nm light for 1 h, Yellow: 20 ppm
163 SWCNT + 10 µM dopamine exposed to no light for 1 h). See fig. S13 for details and instrument exports.
164

165 The electrochemical properties of catecholamines have traditionally been exploited for their
166 characterization and quantification using techniques such as amperometry, cyclic voltammetry, and liquid
167 chromatography with tandem mass spectrometry.[33-35] Similarly, optical modulations in some SWCNT-
168 based sensors have been shown to be driven by the redox activities of their target analytes, with
169 electrochemical mechanisms posited as the basis for fluorescence modulation.[36-38] Given our observation
170 of a wide range of optical responses even in compounds bearing simple catechol motifs, we set out to
171 conduct a deeper exploration of whether the observed optical trends correlated with the electrochemical
172 properties of the screened molecules. Specifically, we wanted to know if experimental optical responses
173 correlated with reduction potentials in our selected subset of catechol compounds.
174

175 The standard reduction potentials of substituted catechols have previously been determined through
176 kinetic studies of their one- and two-electron oxidation by tris(1,10-phenanthroline) iron (III).[32,39] From
177 our screening library of 63 compounds, nine compounds overlapped with a library of 15 analytes for
178 which standard reduction potentials were experimentally determined by Pelizzetti et al.[32] For these nine
179 ligands, our analysis unveiled a robust correlation between reduction potentials of the substituted
180 catechols and their corresponding optical responses (Fig. 2b). Specifically, compounds that underwent
181 facile oxidation elicited more pronounced optical responses than compounds that were more difficult to
182 oxidize (Fig. 2b). This finding suggested electrochemical properties are significant correlates of optical
183 response, although this observation was based on a relatively small subset of our library. To validate and
184 extend these findings, we aimed to explore whether this observation holds true across the broader range of
185 molecules in our screening library.
186

187 Expanding on the work of Pelizzetti et al., Yamabe and colleagues demonstrated that the reduction
188 potentials of substituted benzene-diols are correlated with the electron donating or withdrawing character
189 of the substituents (X) on the aryl group.[32,39] Specifically, they showed that the HOMO of substituted
190 catechols is composed of two types of interactions between the molecular orbitals (MO) of the parent
191 compound (benzene-1,2-diol, P) and substituent (X). The first interaction, known as HOMO$_P$ – HOMO$_X$,
192 occurs between HOMO of the parent molecule (HOMO$_P$) and the HOMO of the substituent (HOMO$_X$).
193 The second interaction involves HOMO$_P$ and lowest unoccupied molecular orbital (LUMO) of the
194 substituent (LUMO$_X$), known as the HOMO$_P$ – LUMO$_X$ interaction. The electron donating or
195 withdrawing nature of the substituent X determines which combination of MOs, HOMO$_P$ – HOMO$_X$ or
196 HOMO$_P$ – LUMO$_X$, predominates in controlling the HOMO of the substituted compound. Yamabe et al.
197 show that for electron donating groups, HOMO$_P$ and HOMO$_X$ have a strong orbital interaction, and the
198 resultant energy splitting opens a large energy gap that raises the energy level of the HOMO of the overall
199 molecule, making it relatively easier to oxidize. In contrast, for electron withdrawing groups, HOMO$_P$ –
200 HOMO$_X$ interactions are insignificant, and HOMO$_P$ – LUMO$_X$ interactions are important for setting the
201 HOMO level of the overall molecule, lowering the HOMO level of the substituted molecule relative to the
202 parent molecule (i.e., benzene-1,2-diol), thus making the molecule more difficult to oxidize. Using this
203 theoretical framework, Yamabe et al. show a strong linear correlation between the experimentally
204 determined reduction potentials of substituted benzene-1,2-diols and computationally determined HOMO
205 levels (e$_{HOMO}$). This correlation highlights that the electron donating or withdrawing character of

6

substituents and computationally obtained e_{HOMO} levels are excellent predictors of reduction potentials for substituted benzene-1,2-diols. This study therefore enabled extending the correlation analysis between optical response and electrochemical properties to a broader range of the screened analytes where reduction potentials had not have been experimentally determined but could be reasonably approximated with substituent inductive constants or computationally determined e_{HOMO} values.

A key finding from the study by Yamabe et al. is that electron donating groups raise the e_{HOMO} values of benzene-1,2-diols, making them easier to oxidize. Accordingly, we first extended our correlation analysis between optical modulation and reduction potentials to the 18-compound subset library (Fig. 2a). Here, we used the Hammett constant of each substituent as a correlate for reduction potential. The analysis unveiled a robust correlation between experimentally measured optical modulations and the Hammett values of each substituent. Specifically, electron donating substituents produced stronger optical modulations (Fig. 2c, fig. S4, fig. S5a). Moreover, for the same substituent *X*, Yamabe et al. demonstrated that the atomic orbital coefficients at the *para*-positions (4 or 5) are larger than the *meta-/ortho*-positions (3 or 5), leading to more robust orbital interactions that strongly modulate HOMO levels. For instance, placement of an -OH group at the *para*-position of benzene-1,2-diol (**C**) significantly increases electron density in the aryl compared to placement at the *meta-/ortho*-position (**MM**), making the molecule more easily oxidizable (fig. S4a). Notably, the optical responses we measured correlated well with such subtle differences between isomers of the same compound (fig. S4a,b) and in compounds that differed in just one functional group (fig. S4c,d). Because Yamabe's framework ultimately implicates e_{HOMO} values as correlates for reduction potentials, it allowed us to extend this analysis to molecules in our library lacking a simple catechol motif or for which Hammett values could not be found, but for which overall HOMO values can be computed.

Consequently, correlations between optical modulations and computationally determined e_{HOMO} levels were examined for various subsets of the screened analytes. Here too, a robust correlation was observed between optical responses and HOMO levels for the 18 compound sub-library (fig. S6a), as well as various other subsets (fig. S6b) and the entire library of compounds (fig. S6,c). Importantly, while correlation between HOMO and optical responses was strong, high e_{HOMO} levels do not guarantee an optical response (fig. S6c,d). Consistent with our earlier heuristic description, these results show that at least two vicinal hydrogen bond donating groups are necessary for optical modulation in addition to the observed correlations with electron densities on the aryl group (fig. S6e). In most cases, these groups are *ortho-* to each other but they can be connected through extended conjugation as well (e.g., **4**, fig. S6e).

Next, we investigated whether oxidized catechol products could be detected when these compounds were exposed to ssDNA-SWCNT conjugates, as suggested by the correlations presented in the foregoing analysis. We first used an enzyme-linked immunosorbent assay (ELISA) that can sensitively quantify concentration of dopamine at picomolar concentrations but is otherwise insensitive to quinones, the oxidative product of catechols (fig. S7). Oxidation of dopamine with sodium periodate[40] induced rapid depletion of the starting material, which we verified with the ELISA assay (Fig. 2d). We then quantified the level of oxidation of dopamine in solutions that had been exposed to ssDNA-SWCNT conjugates for various durations and excitation laser intensities. Surprisingly, no oxidation product was detected using this assay, indicating minimal oxidation of dopamine in the starting material (Fig. 2d). Similarly, high-performance liquid chromatography (HPLC) detection of quinones showed depletion of starting material in periodate controls (Fig. 2e, dopaquinone (DQ)) but not in experimental solutions (Fig. 2e, DA/SWCNT/Excited, DA/SWCNT/ Not Excited).

Oxidation of benzene-diols proceeds through a one-electron abstraction to form a semi-quinone radical[41], and we reasoned that if a radical is formed during the process of generating optical modulations, highly

7

reducing reagents should attenuate or eliminate these optical responses. Similarly, if electron transfer reactions occur, dissolved molecular oxygen could act as an electron sink or play a role as an intermediate in a putative electrochemical reaction, generating reactive oxygen species. We observed no attenuation in optical response in the presence of reducing reagents and reactive oxygen scavengers, consistent with the absence of oxidation from ELISA and HPLC measurements (Supplementary Fig. S8). In sum, our findings indicate that redox reactions involving dissolved molecular oxygen or single electron transfers that generate radicals are unlikely to be present. Previous studies have similarly showed that reactive oxygen species are unlikely to be involved during catecholamine molecular recognition.[11] We therefore conclude that although optical responses showed a strong correlation with the electrochemical properties of benzene-1,2-diols, the evidence indicates that the analytes themselves are not undergoing oxidation during the process of optical modulation of ssDNA-SWCNT conjugates.

In our experiments, we observed that solution pH, a key experimental variable, could have a significant and yet underappreciated impact on the magnitude of the measured optical modulations. The influence of pH on SWCNT optical properties is well documented, with a general increase in brightness noted for most SWCNT solutions as pH increases.[42,43] However, the effect of pH on analyte-induced optical modulation is not well understood. We found that changing solution pH by just two units could dramatically attenuate optical response for some analytes (Fig. 3a). These analytes have substituents with pK_A values that allow deprotonation to occur in this range. To probe pH effects more systematically, we measured the optical responses of a subset of analytes while ranging solution pH from 2 to 13 units (Fig. 3b, fig. S9). At high pH levels (> 8), optical responses were greatly diminished for all analytes. This reduction is partly a consequence of the fact that nanotube fluorescence (i.e., brightness) increases with increasing pH, reducing the dynamic range of the optical response that can be elicited by the analytes. In other words, the baseline fluorescence (F_0) is higher, making the change in fluorescence ($\Delta F/F_0$) lower. This can be thought of as pH setting the baseline brightness, F_0, and ligand addition determining the final brightness, F. However, the maximum brightness induced by some benezene-1-2-diol derivatives in our screen was significantly higher than the brightness of nanotubes at high pH, suggesting that pH-induced brightness saturations and consequent lowering of sensor dynamic range cannot explain sensor pH dependencies (Fig. 3b, fig. S9). Indeed, the diminution of $\Delta F/F$ as a function of pH showed a different trend in all the species whose optical responses were measured as a function of pH, with some analytes undergoing rapid decrease in their ability to generate optical response (e.g., **F**, Fig. 3b), while other substrates exhibited broader pH tolerance (e.g., **DA**, Fig. 3b). Since the same ssDNA-SWCNT complex is used for all analytes, the pH dependencies we see are unlikely to be driven by changes in the photophysical properties of nanotubes and their conjugated ssDNA. We hypothesized that these differences are intrinsic to the analytes. Importantly, pH-dependent trends correlated with deprotonation of the analytes, as predicted by the pK_A of the substituents on the aryl group. This suggests that the deprotonated species may interact with ssDNA-SWCNT conjugates differently from the parent species (Fig. 3c,d). We therefore conclude that optical modulations in ssDNA-SWCNT conjugates generated by benzene-1,2-diol and its derivatives exhibit a sensitivity to molecular charge, in addition to correlations with electrochemical properties we presented in the foregoing analysis. This result suggested that the dynamics of interaction between analytes and ssDNA-SWCNT supramolecular complex, mediated by a combination of molecular structure and charge, likely play a key role in coordinating the optical response process in molecules that have favorable electrochemical profiles (e_{HOMO}). While we used (GT)$_6$-SWCNTs conjugates for this study, similar results were obtained using (GT)$_{15}$-SWNCTs for a subset of compounds (fig. S10), suggesting that the results can be generalized to the (GT)$_N$-SWCNT family of sensors.

Fig. 3. Effect of solution pH on ΔF/F for several compounds. a, Four example compounds that exhibit different responses at low (pH ~6) and high (pH ~8) solution pH; ΔF/F values (mean) were normalized against response at pH ~6. **b,** Responses in compounds in (**a**) measured across a range of pH. For analytes where fluorescent response was less than baseline (i.e., $F-F_0 \leq 0$), higher pH values were not further explored. **c,** pK_A model of **F** showing proportions of microspecies at different pH. **d,** Comparison of **F** (purple with error bars) and **DA** (blue with error bars) ΔF ($F-F_0$) values as a function of pH, juxtaposed against microspecies transition profiles from $-NH_3^+$ to $-NH_2$ (solid lines without error bars in the same respective colors). Note the pK_A values for the protonated amine in F^+ and DA^+ shown as red numerical text adjacent to the functional group.

We next employed molecular dynamics (MD) simulations to rationalize our experimental findings and gain detailed atomic and molecular insight into molecular interactions in ssDNA-SWCNT conjugates, and how these correlate with experimentally observed optical modulations. We focused on a subset of 14 analytes using MD simulations (Methods). Dopamine (**DA**) was selected as the key model analyte for our computational studies, consistent with our experimental approach. The remaining analytes spanned the full spectrum of experimentally observed optical responses. Specifically, the simulated molecules included the analytes **F**, **C**, and **O** which elicited stronger fluorescence responses than dopamine, and analytes **T** and **1**, which showed weaker responses. Analyte **Y**, which had a roughly similar response to dopamine, was also included. To explore pH effects, we modeled additional molecules in their dominant protonation states at selected pH values (fig. S11). These included F^+ (at pH = 5), **RR** (at pH = 7), RR^+

9

(at pH = 3), $\mathbf{YY^+}$ (at pH = 7), $\mathbf{O}$ (at pH = 7), $\mathbf{O^+}$ (at pH = 3), $\mathbf{5^+}$ (at pH = 7), and $\mathbf{C^-}$ (at pH = 11). We determined molecular charge using ChemAxon Chemicalize[44] modeling of pK_A, matched to the pH conditions used during experimental measurements. Each simulated system contained six molecules of the selected analyte, which were allowed to diffuse freely and interact with 4 nm segment of (9,4)-SWCNT chirality wrapped by three strands of $(GT)_6$ ssDNA oligonucleotides, immersed in 0.10 M aqueous NaCl solution (Methods). The systems were simulated for 6 µs to observe multiple binding and unbinding events of analyte molecules on the ssDNA-SWCNT conjugate surface.
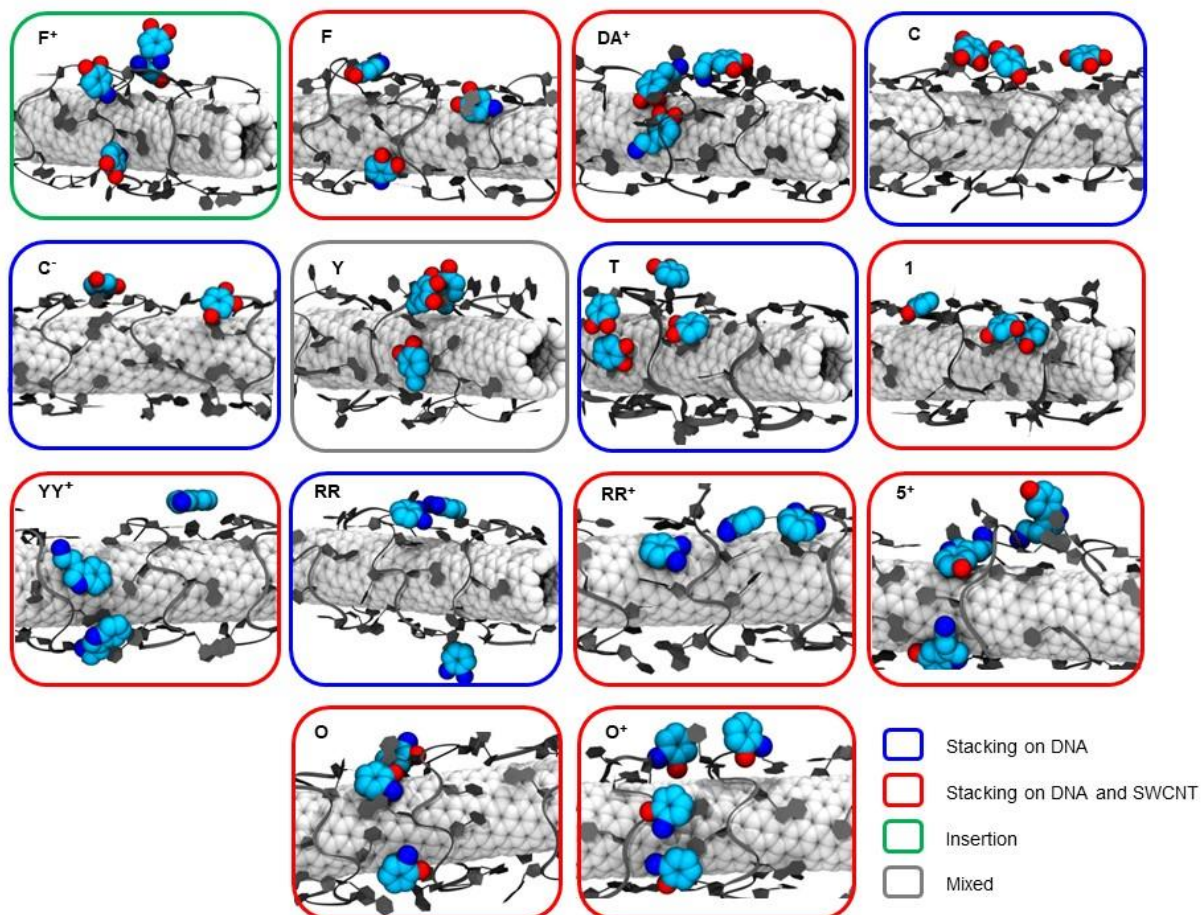
Fig. 4. Predominant binding modes of 14 selected analytes with the ssDNA-SWCNT conjugate and the SWCNT surface observed in MD simulations. The SWCNT carbon atoms are shown as white spheres, the $(GT)_6$ ssDNA strands are shown as dark grey ribbons, and the analyte molecules heavy atoms are shown as van der Waals spheres (C: cyan, N: blue, O: red). The hydrogen atoms have not been shown for clarity. Snapshot frame colors correspond to the predominant binding mode observed for the analyte, as defined in the legend. The mixed mode (grey) indicates that there is no predominant binding mode, but the analyte molecules exhibit a mixture of both stacking and insertion interactions.

We began by cataloging all the predominant binding modes observed when the selected analytes interacted with ssDNA-SWCNT molecular complexes. Figure 4 shows representative snapshots of the preferred binding modes of the 14 selected analytes studied. The observed binding modes fall into two categories: analytes either stacked either directly on top of ssDNA nucleotides functionalizing the SWCNT or stacked on the exposed segments of the SWCNT surface. Specifically, the molecules $\mathbf{C}$, $\mathbf{C^-}$, $\mathbf{T}$ and $\mathbf{RR}$ were primarily observed stacking on the ssDNA nucleotides, while molecules $\mathbf{F}$, $\mathbf{DA^+}$, $\mathbf{RR^+}$, $\mathbf{O}$, $\mathbf{O^+}$, $\mathbf{5^+}$, $\mathbf{1}$ and $\mathbf{YY^+}$ stacked on both ssDNA and SWCNT surface. Interestingly, $\mathbf{F^+}$ favored a distinct insertion mode rather than stacking, although brief instances of sideway stacking on ssDNA bases were

10

343 occasionally observed (Fig. 4). Lastly, analyte **Y** did not exhibit a single predominant binding mode but
344 rather interacted with ssDNA-SWCNT through a combination of binding modes.
345
346 It is noteworthy that π-stacking is an anticipated binding mode for the molecules we studied, largely
347 because a central feature of their molecular structure is an aryl group, which tends to stack on ssDNA
348 bases and the graphitic lattice of SWCNTs. The binding modes we observed align with our previous
349 computational work, where dopamine was shown to stack on surfaces of SWCNTs and ssDNA-
350 SWCNTs.[12] In this study, we further observed that the identity and positioning of functional groups
351 around the central aryl motif influenced the preferred binding modes of the analytes. We attribute this to
352 the fact that polar functional groups typically engage in directional interactions, and this influences the
353 overall orientations of the analytes on nanotube surfaces. A common observation for analytes with
354 positively charged -NH_3^+ groups (**F$^+$**, **DA$^+$**, **YY$^+$**, **RR$^+$**, **O$^+$**, **5$^+$**) is their propensity to interact with the
355 ssDNA phosphate backbone (fig. S12a-d). Among these, dopamine (**DA$^+$**) exhibited the strongest
356 tendency to participate in this type of binding interaction. This directional interaction between the
357 positively charged amine groups and negatively charged ssDNA phosphate backbone is a key factor
358 determining the predominant binding modes in all the positively charged molecules. Since the protonation
359 state of amine groups is pH-dependent, these findings help explain our experimental observation that pH
360 is a critical extrinsic factor influencing fluorescence responses.
361
362 The neutral molecules (**F**, **T**, **Y**, **1**, **RR**, **C**, **O**) and the negatively charged molecule (**C$^-$**) exhibit transient
363 binding behavior, making it difficult to identify the primary factors governing their binding behavior. A
364 comparison of **DA$^+$** and **T** binding to the SWCNT surface over time is shown in fig. S12e. Despite the
365 transient nature of these interactions, hydrogen bonds between the -OH or -NH_2 functional groups and the
366 oxygen atoms of the ssDNA sugar-phosphate backbone, or the nitrogen atoms of the ssDNA bases, are
367 frequently observed (as seen, for example, in the binding pose for **C** shown in Fig. S12c). In summary,
368 based on a visual inspection of the simulation trajectories, we hypothesize that the functional groups
369 present in these analytes primarily dictate the preferred binding mode of ligands.
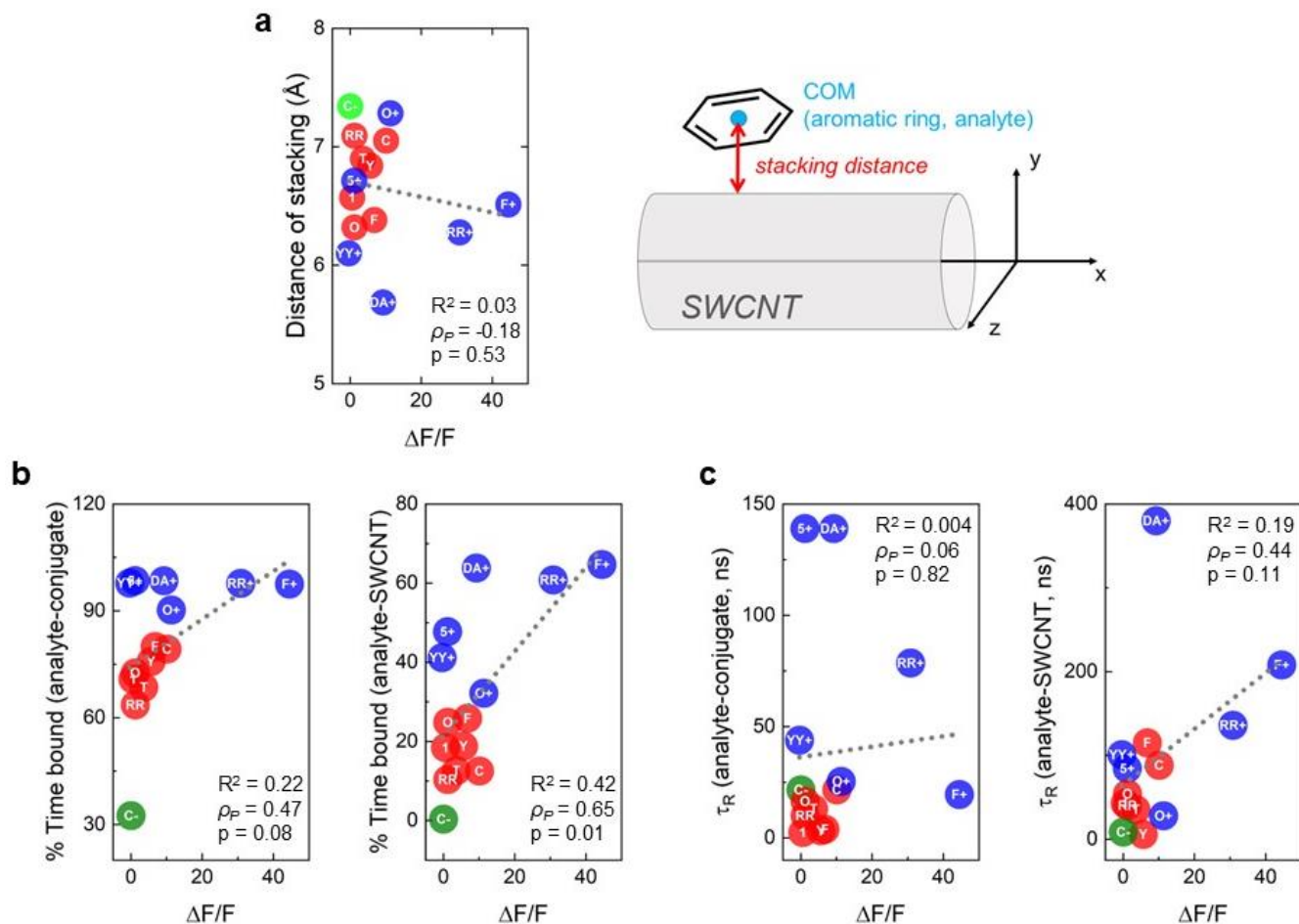
Fig. 5. Correlation analysis between MD simulation-derived parameters and experimentally measured optical sensor responses $\Delta F/F$. a, Scatter plot of the average stacking distance of analytes and their $\Delta F/F$ values (mean). The scheme on the right defines the instantaneous stacking distance for the analytes as the shortest distance between the center of mass (COM) of the analyte's aryl motif and the nanotube surface. The reported distances are averaged only over frames in which the analyte is stacking on the surface within 10 Å and averaged over the six analyte molecules. **b,** Scatter plots of the percent of time analytes are bound to either ssDNA-SWCNT conjugate (left) or the nanotube surface (right) and $\Delta F/F$ values corresponding to these analytes. **c,** Scatter plot of the residence times of analytes when bound to either ssDNA-SWCNT conjugate (left) or the nanotube surface (right) and $\Delta F/F$ values corresponding to these analytes. In all the plots, scatter points for positively charged, neutral, and negatively charged analytes are shown in blue, red, and green, respectively. The linear regression corresponding to the best fit is shown as a grey dotted line in every plot. The R^2 coefficients, Pearson correlation coefficients (ρ_P) and p-values (p) are reported in each plot.

We next employed extended MD simulations to obtain quantitative parameters that characterize atomistic behavior and binding of the selected analytes, and performed a correlation analysis between these parameters and the experimentally measured optical responses. Several parameters were computed from the MD simulations for this correlation, including the average distance of each analyte's aryl ring from the SWCNT surface (as defined in Fig. 5a), the percentage of time each analyte spent binding to the ssDNA-SWCNT conjugate or directly to SWCNT surface during a given simulation period, and the residence times of each analyte's interaction with either the SWCNT surface or the entire ssDNA-SWCNT conjugate. Our goal was to determine which of these simulation parameters, along with the experimental correlates we identified, collectively quantify a "perturbation cross section" for each analyte, defined as the ability of each analyte to perturb the local chemical environment of the nanotube and elicit an optical response.

12

394 Figure 5 summarizes of the results of the correlation analyses between the MD-derived parameters and
395 experimentally measured $\Delta F/F$ values. Our analysis showed a weak negative correlation between the
396 stacking distance and $\Delta F/F$ ($R^2 \sim 0.03$, Pearson correlation coefficients, $\rho_P = -0.18$, with a non-significant
397 p-value, Fig. 5a). The negative correlation suggests that the closer the aryl ring is to SWCNT surface, the
398 higher the $\Delta F/F$ value, consistent with the notion that optical response is a consequence of an analyte's
399 ability to perturb the local environment of the SWCNT. Although this trend did not rise to the level of
400 statistical significant, a grouped analysis between the positively charged molecules from our set of 14
401 analytes (**F⁺, DA⁺, YY⁺, RR⁺, 5⁺, O⁺**) and the neutral analytes (**F, C, Y, T, 1, RR, O**), showed that the
402 positively charged molecules bind significantly closer the SWCNT surface. This was confirmed by a p-
403 value of 0.02 from an unpaired t-test between the two groups. This finding is consistent with the full
404 simulation trajectory noted in Fig. S12e for DA+ and T.
405
406 Moreover, we observed a weak positive correlation between the total percentage of time the analyte
407 molecules are bound to the ssDNA-SWCNT conjugate during 6 μs simulation trajectories and $\Delta F/F$
408 values ($R2 \sim 0.22$, Pearson correlation coefficients, $\rho_P = 0.47$, with a non-significant p-value, Fig. 5b).
409 This correlation suggests that the more time analytes spend bound to the ssDNA-SWCNT conjugate, the
410 higher the $\Delta F/F$, which aligns with the idea that more analyte-biosensor interactions lead to enduring
411 perturbations to the local environment of the SWCNT. Although this correlation was not statistically
412 significant, a stronger and statistically significant positive correlation ($R^2 \sim 0.42$, Pearson correlation
413 coefficients, $\rho_P = 0.65$, $p = 0.01$) was observed between the percentage of time analytes remained bound
414 to the SWCNT surface and $\Delta F/F$ values. This finding is consistent with the expectation that longer
415 analyte-SWCNT interaction times are associated with stronger "perturbation cross sections" for analytes,
416 more so than binding to the ssDNA-SWCNT corona alone (Fig. 5b). The positively charged analytes in
417 our study (**F⁺, DA⁺, YY⁺, RR⁺, 5⁺, O⁺**) spent significantly higher percentage of the simulation time bound
418 to SWCNT than the neutral molecules (**F, C, Y, T, 1, RR, O**) and the single negatively charged analyte
419 examined (**C⁻**, Fig. 5b) ($p = 0.002$ on unpaired t-test). We attribute the longer binding times to favorable
420 interactions between the positively charged $-NH_3^+$ groups and the ssDNA phosphate backbone.
421 In addition to examining fraction of time the analytes spent bound to the SWCNT surface or ssDNA-
422 SWCNT conjugate, we also studied the relationship between binding residence times, defined as average
423 residence times across all bounding poses, and $\Delta F/F$ values. Binding residence helps differentiate between
424 stably bound analytes and those that exhibit transient but frequent binding interactions, both of which
425 contribute to total bound time. This analysis showed a very weak correlation ($R^2 \sim 0.004$, Pearson
426 correlation coefficients, $\rho_P = 0.06$, with a significant p-value) between the residence time of these analyte
427 molecules in their binding poses on the ssDNA-SWCNT conjugate and the $\Delta F/F$ (Fig. 5c). However, a
428 stronger positive correlation was observed between the analyte residence times at the SWCNT surface and
429 the $\Delta F/F$, ($R^2 \sim 0.19$, Pearson correlation coefficients, $\rho_P = 0.44$, with a non-significant p-value, Fig. 5c,
430 right panel). This finding can be rationalized by the expectation that longer residence times are positively
431 correlated with stronger "perturbation cross section" for each analyte. Among the positively charged
432 molecules from our set of analytes (**F⁺, DA⁺, YY⁺, RR⁺, O⁺, 5⁺**), all except **YY⁺, 5⁺**, and **O⁺** exhibited
433 significantly higher residence time than the neutral molecules (**F, C, Y, T, 1, RR, O**). This was confirmed
434 by the p-value of 0.001, obtained from an unpaired t-test on positively charged versus neutral molecules.
435 The fact that **YY⁺, 5⁺**, and **O⁺** had residence times similar to those of neutral molecules implies that the
436 molecules preferentially associated with the ssDNA-SWCNT conjugate than the SWCNT surface for
437 majority of the simulation. However, unlike the other positively charged molecules, their binding
438 interactions were less stable, which led to shorter residence times. Importantly, these analyses reveal that
439 binding does not predict an analyte's ability to elicit an optical response, as is evident from the binding
440 results of **YY+,** which elicited no optical response in experimental measurements, but exhibits robust
441 binding behavior in MD simulations (Figure 5).

13

We further explored whether "perturbation cross sections" of analytes are influenced by the proximity of polar functional groups of the analytes close to nanotube surfaces. This exploration was motivated by previous studies demonstrating that the dielectric constant of the nanotube's environment significantly impacts SWCNT photophysics.[2] For example, Silvera-Batista and colleagues showed that increasing the dielectric constant of SWCNT environment from 2 to 5 by changing solvents could reduce the photoluminescence intensity by more than 50%.[45] Building on these findings, we investigated whether the polar functional groups of each analyte, when in close proximity to the nanotube surface, could perturb the electrostatic field around the ssDNA-SWCNTs and thus influence their optical properties.
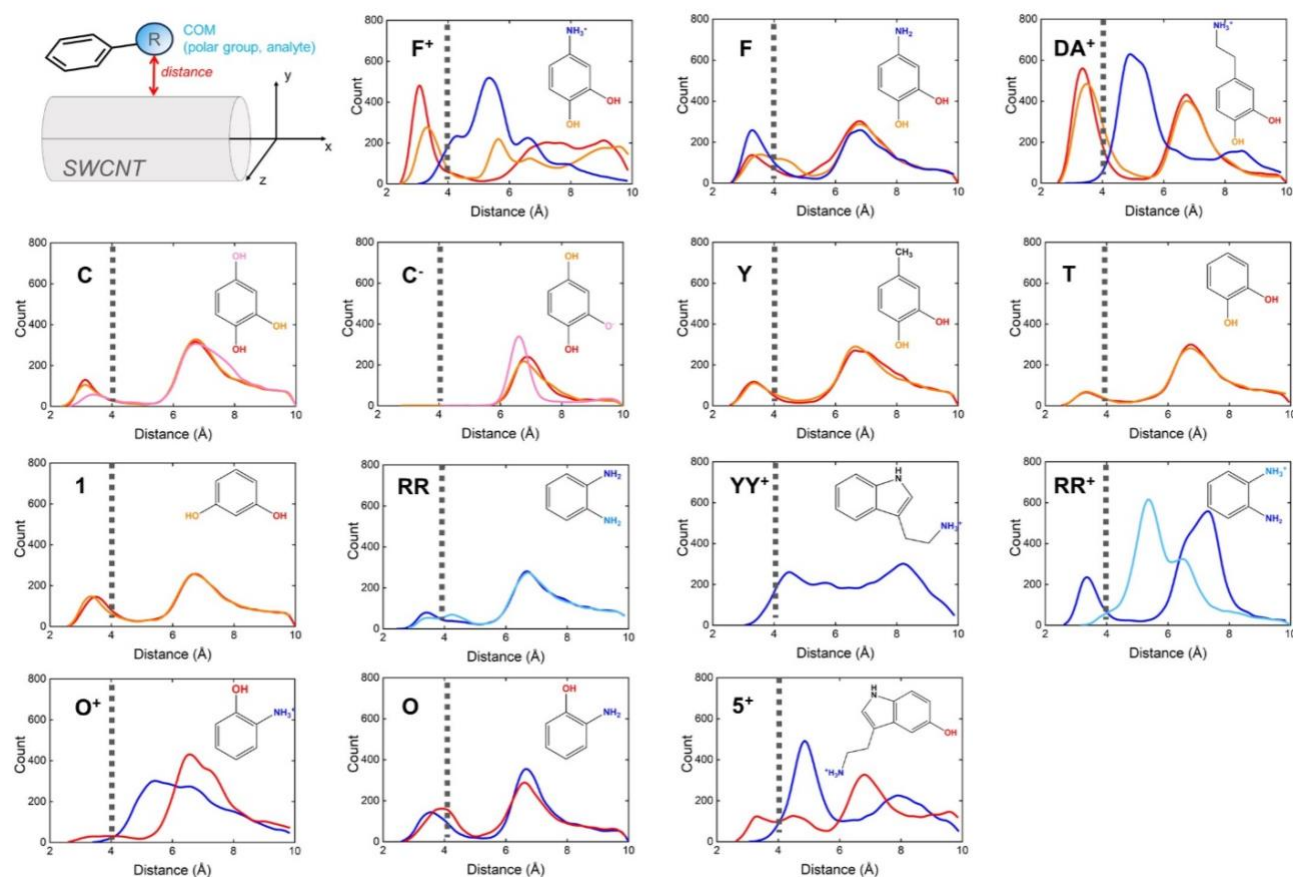
Fig. 6. Probability distribution of analyte polar groups distances from nanotube surfaces. The distances were defined as the shortest distances between the center of mass (COM) of each analyte polar groups and the nanotube surface, as schematically shown in the top left panel. The distributions consider all six molecules of analyte and only those frames where the distances are within 10.0 Å. The lines representing amino groups are shown in shades of blue, and the lines representing hydroxy groups are shown in shades of red. The grey dotted line at 4.0 Å marks a rough threshold distance to indicate a direct close interaction between the polar group and nanotube.

Towards this goal, we measured the distances between the center of mass (COM) of each analyte's polar functional groups and the nanotube surface in all MD simulations, focusing on trajectory frames in which the groups were found within 10.0 Å of the nanotube surface. The observed distances were then used to generate probability distributions of the distances between analyte polar groups and SWCNT surfaces (Fig. 6). For instance, the molecule **F⁺** has two polar functional groups: -OH and -NH₃⁺. An examination of its probability distribution shows that hydroxyl groups have a high probability of being within 3.0-4.0 Å away from the SWCNT surface, whereas the protonated amine has a peak at ~ 5.2 Å away from the nanotube surface. In contrast, the neutral molecule **F** showed similar distance distributions for its hydroxyl groups, but the amine group was closer to the nanotube surface, with a maximum at 3.5 Å. This

14

466 data is consistent with the analyte binding modes discussed earlier, where $\mathbf{F}^+$ molecules exhibiting an
467 insertion mode of binding, with the protonated amine sometimes projecting away from the nanotube
468 surface. On the other hand, $\mathbf{F}$ molecules tended to stack on the ssDNA corona or the nanotube surface,
469 with both the -OH and -NH$_2$ groups at similar distances from the surface. $\mathbf{DA}^+$ molecules were observed
470 to lie flat on the nanotube surface, but the protonated amine group, located two carbon centers away from
471 the aryl ring, projected upward and away from the nanotube surface, interacting with the negatively
472 charged ssDNA. This binding observation is consistent with the polar group distribution profiles (Fig. 6).
473
474 RR+ has two polar groups: -NH2 and -NH3+. The neutral amine shows a moderate probability of being
475 near the nanotube surface (maximum at 3.4 Å) and a higher probability of being farther away (maximum
476 at 6.4 Å). In contrast, the protonated amine has a one large peak at 5.4 Å. For molecule RR with two
477 neutral amine groups, the distribution is similar for both, with a maximum at 6.4 Å. For $\mathbf{O}^+$, the
478 protonated amine is closer to the nanotube (maximum at 5.4 Å) than the neutral -OH group (maximum at
479 6.6 Å). In the neutral molecule $\mathbf{O}$, the two polar groups have similar distribution. For $\mathbf{C}$ and $\mathbf{C}^-$,
480 deprotonation of one of the ortho -OH groups in $\mathbf{C}$ results in a drastic rearrangement in distribution, with
481 all polar groups in $\mathbf{C}^-$ more than 6.0 Å away from the nanotube surface. Molecules $\mathbf{Y}$, $\mathbf{T}$, and $\mathbf{1}$ all exhibit
482 a similar distribution pattern, with moderate probabilities at ~ 3.5 Å from the nanotube surface, and much
483 higher probabilities farther away (~ 6.5 Å). Between the isomers $\mathbf{T}$ and $\mathbf{1}$, the -OH groups in $\mathbf{1}$ have
484 slightly higher probability of being closer to the nanotube surface than those in $\mathbf{T}$. For $\mathbf{YY}^+$ molecules, the
485 polar -NH$_3^+$ group is situated two carbon centers away from the indolamine. Consequently, stacking on
486 the nanotube surface leads to the polar group being projected away from the nanotube surface, similar to
487 the behavior of $\mathbf{DA}^+$ molecules. A similar observation is noted for the -NH$_3^+$ group in $\mathbf{5}^+$. These findings
488 provide understanding of how different analytes interact with the nanotube, placing an emphasis on the
489 spatial distribution of polar functional groups relative to the nanotube surface.
490

Discussion

492 Optical biosensors facilitate advances in various disciplines of biological research by enabling the
493 exploration of questions that are difficult to address with other methods. While many optical biosensors
494 are based on genetically engineered proteins, synthetic optical sensors have also made important
495 contributions. Among these synthetic biosensors, SWCNTs possess useful photophysical attributes that
496 make them particularly well-suited for applications in biology.[1] SWCNT-based biosensors have been
497 developed for a wide range of analytes, including reactive oxygen species[10,46], small biomolecules and
498 lipids[11,13,16,47], neuropeptides[14], proteins[48-50], disease biomarkers[51,52], and even bacteria and viruses[53,54].
499

500 Despite the growing list of analytes for which SWCNT-based sensors have been developed, the
501 mechanisms behind their molecular recognition and optical modulation remain poorly understood. In this
502 work, we studied (GT)$_6$-SWCNT bio-nano hybrids, which exhibit vigorous fluorescence modulation when
503 exposed to catecholamines, a family of biologically important small molecules. Our goal was to enhance
504 the understanding of sensor optical modulation by systematically exploring the relationship between
505 ligand properties and optical responses. We complemented our experimental findings with MD
506 simulations to rationalize our experimental observations and gain valuable insights.
507

508 Our experiments demonstrated that the electron densities of the aryl rings in catechols positively
509 correlated with the amplitude of their optical response. Electron deficient catechols typically elicit lower
510 optical responses compared to electron rich ones (Fig. 2, Fig. S4). Given the strong correlation between
511 catechol electron densities and their reduction potential, we investigated whether the oxidation of
512 catechols and subsequent electron transfer to nanotubes might underlie the observed optical modulation.
513 However, we found that catechols do not undergo oxidation when exposed to excited ssDNA-SWCNT

conjugates, suggesting that a transient perturbative process, rather than permanent charge transfer, is more likely for the optical modulation. Through a systematic exploration of the derivatized catechols and related compounds, we identified aminocatechols and phenylenediamines as substrates that can elicit robust optical responses from ssDNA-SWCNT conjugates, thereby expanding the substrate scope detectable by $(GT)_N$-SWCNT bio-nano conjugates. Moreover, we observed that the optical response of certain analytes was highly sensitive to solution pH, indicating that the protonation state (charge) of the various substituents on the aryl group play a key role in the molecular recognition and optical modulation process.

Optical biosensors fall into two major groups: those based on molecular recognition and those based on chemical reactivity, known as activity-based sensing.[55] While traditional optical biosensors typically rely on a lock-and-key type molecular recognition process, activity-based sensors detect molecular reactivity between the sensor and analyte.[55,56] Regarding ssDNA-SWCNT catecholamine sensors, our data indicated a strong correlation between catechol redox activity and optical response, suggesting an activity-based model may be a fit. However, the absence of detectable oxidized catechol products was not fully consistent with this model.

To gain better understanding and develop an integrated model of sensor function, we employed molecular dynamics (MD) simulations. Our goal was to first characterize stable binding modes between a carefully selected group of analytes and ssDNA-SWCNT conjugates. We then sought to identify analyte-sensor interaction parameters that correlate with experimentally measured optical responses. From binding interactions, we identified two primary modes of association between analytes and ssDNA-SWCNT conjugates: stacking on ssDNA bases and stacking on nanotube surfaces. In both cases, we found that molecular charge strongly influenced the stacking stability of the molecules, which explains the sensor's pH dependence observed experimentally. Specifically, positively charged substituents (amines) strongly interact with ssDNA phosphate groups, affecting both stability of binding and binding residence times.

However, some analytes with positively charged amine groups could exhibit relatively stable binding through interactions with ssDNA phosphate groups, but elicited small (e.g., 5+) or no (e.g., YY+) optical response. Conversely, some analytes without charged amine groups (e.g., **C**) were able to generate a strong optical response. This indicated that the perturbation cross section of an analyte is not a simple function of its ability to bind to ssDNA-SWCNT conjugates through electrostatic interactions. Instead, the characteristics of substituents on the aryl group plays an important role, consistent with experimental observation that substituents significantly influence optical response. Further analysis revealed that proximity of polar substituents to nanotube surfaces correlated positively with optical response. This indicates that molecules that have a high perturbation cross section (e.g., **DA⁺**, **F⁺**) not only stably bind ssDNA-SWCNT conjugates but exhibit higher density of polar substituents close to the nanotube surface (Fig. 6).

Therefore, MD simulations show that stable molecular binding is essential for eliciting an optical response. In this regard, ssDNA-SWCNT sensors are similar to traditional biosensors that function through molecular recognition and ligand binding. The binding interactions predominantly involve two types: electrostatic interactions through charged groups and π-stacking interactions, the former facilitating and contributing to the stability of the later. However, unlike traditional biosensors, stable ligand binding alone is not sufficient to elicit a response. The perturbation cross section of a ligand depends on the nature of substituents on the aryl ring (electron donating vs. withdrawing) and their proximity to the surface of the nanotube when the ligand is in a stable binding mode (Fig. 6).

16

Several explanations could account for the observed dependence of sensor response on the electron donating or withdrawing character of the substituents. One possibility is that electron donating substituents enhance the π-stacking stability of the aryl ring on the nanotube surface, consistent with well-known substituent effects on π-interaction between aromatic rings.[57] This stable stacking may more efficiently displace water molecules from the nanotube surface, transiently reducing the surface dielectric constant and thereby increasing optical output. This hypothesis is supported by previous findings, where we showed that dopamine binding outcompetes sodium cholate binding to nanotube surfaces in ssDNA-SWCNT conjugates.[12] Another potential explanation is that stably bound and electron rich aryl motifs could coordinate with deleterious surface defects, locally and transiently altering nanotube bandgap, which could increase optical output. Alternatively, electron rich substituents themselves, instead of the π-stacked aryl group, may be responsible for displacing water or transiently mitigating the effect of surface defects, thus enhancing the nanotubes' brightness. These potential mechanisms highlight the complexity of interaction between analytes and ssDNA conjugated nanotubes, suggesting that multiple factors contribute to sensor response. In conclusion, our findings indicate that optical responses in ssDNA-SWCNT conjugates depend both on molecular bindings events, similar to traditional optical sensors, and the chemical properties (structure, charge, electron density) of the analyte, similar to activity-based sensing models. These findings may offer avenues for tuning the performance of existing sensors or guiding the development of new ones through designed ssDNA modifications that improve analyte binding.

References and Notes

1   Krasley, A. T. *et al.* Carbon Nanomaterial Fluorescent Probes and Their Biological Applications. *Chemical Reviews* **124**, 3085-3185, doi:10.1021/acs.chemrev.3c00581 (2024).

2   Gao, Z. Advances in surface-coated single-walled carbon nanotubes as near-infrared photoluminescence emitters for single-particle tracking applications in biological environments. *Polymer Journal* **50**, 589-601, doi:10.1038/s41428-018-0052-8 (2018).

3   Jin, H., Heller, D. A. & Strano, M. S. Single-Particle Tracking of Endocytosis and Exocytosis of Single-Walled Carbon Nanotubes in NIH-3T3 Cells. *Nano Letters* **8**, 1577-1585, doi:10.1021/nl072969s (2008).

4   Paviolo, C. *et al.* Near-Infrared Carbon Nanotube Tracking Reveals the Nanoscale Extracellular Space around Synapses. *Nano Letters* **22**, 6849-6856, doi:10.1021/acs.nanolett.1c04259 (2022).

5   Godin, A. G. *et al.* Single-nanotube tracking reveals the nanoscale organization of the extracellular space in the live brain. *Nature Nanotechnology* **12**, 238-243, doi:10.1038/nnano.2016.248 (2017).

6   Ackermann, J., Metternich, J. T., Herbertz, S. & Kruss, S. Biosensing with Fluorescent Carbon Nanotubes. *Angewandte Chemie International Edition* **61**, doi:10.1002/anie.202112372 (2022).

7   Kruss, S. *et al.* Carbon nanotubes as optical biomedical sensors. *Advanced Drug Delivery Reviews* **65**, 1933-1950, doi:10.1016/j.addr.2013.07.015 (2013).

8   Zhang, J. *et al.* Single molecule detection of nitric oxide enabled by d(AT)15 DNA adsorbed to near infrared fluorescent single-walled carbon nanotubes. *Journal of the American Chemical Society* **133**, 567-581, doi:10.1021/JA1084942 (2011).

9   Kim, J.-H. *et al.* The rational design of nitric oxide selectivity in single-walled carbon nanotube near-infrared fluorescence sensors for biological detection. *Nature Chemistry* **1**, 473-481, doi:10.1038/nchem.332 (2009).

10   Jin, H. *et al.* Detection of single-molecule H2O2 signalling from epidermal growth factor receptor using fluorescent single-walled carbon nanotubes. *Nature Nanotechnology* **5**, 302-309, doi:10.1038/nnano.2010.24 (2010).

11   Kruss, S. *et al.* Neurotransmitter Detection Using Corona Phase Molecular Recognition on Fluorescent Single-Walled Carbon Nanotube Sensors. *Journal of the American Chemical Society* **136**, 713-724, doi:10.1021/ja410433b (2014).

612   12   Beyene, A. G. *et al.* Ultralarge Modulation of Fluorescence by Neuromodulators in Carbon Nanotubes
613   Functionalized with Self-Assembled Oligonucleotide Rings. *Nano letters* **18**, 6995-7003,
614   doi:10.1021/ACS.NANOLETT.8B02937 (2018).
615   13   Jeong, S. *et al.* High-throughput evolution of near-infrared serotonin nanosensors. *Science Advances* **5**,
616   3771-3789, doi:10.1126/SCIADV.AAY3771 (2019).
617   14   Mun, J. *et al.* Near-infrared nanosensors enable optical imaging of oxytocin with selectivity over
618   vasopressin in acute mouse brain slices. *Proceedings of the National Academy of Sciences* **121**,
619   doi:10.1073/pnas.2314795121 (2024).
620   15   Iverson, N. M. *et al.* In vivo biosensing via tissue-localizable near-infrared-fluorescent single-walled
621   carbon nanotubes. *Nature Nanotechnology 2013 8:11* **8**, 873-880, doi:10.1038/nnano.2013.222 (2013).
622   16   Zhang, J. *et al.* Molecular recognition using corona phase complexes made of synthetic polymers adsorbed
623   on carbon nanotubes. *Nature Nanotechnology* **8**, 959-968, doi:10.1038/nnano.2013.236 (2013).
624   17   Nakatsuka, N. *et al.* Aptamer–field-effect transistors overcome Debye length limitations for small-molecule
625   sensing. *Science* **362**, 319-324, doi:10.1126/science.aao6750 (2018).
626   18   Zhao, M. *et al.* DNA-directed nanofabrication of high-performance carbon nanotube field-effect transistors.
627   *Science* **368**, 878-881, doi:10.1126/science.aaz7435 (2020).
628   19   Lin, Z., Yang, Y., Jagota, A. & Zheng, M. Machine Learning-Guided Systematic Search of DNA
629   Sequences for Sorting Carbon Nanotubes. *ACS Nano* **16**, 4705-4713, doi:10.1021/acsnano.1c11448 (2022).
630   20   Yang, F. *et al.* Chirality Pure Carbon Nanotubes: Growth, Sorting, and Characterization. *Chemical Reviews*
631   **120**, 2693-2758, doi:10.1021/acs.chemrev.9b00835 (2020).
632   21   Lin, Z. *et al.* DNA-guided lattice remodeling of carbon nanotubes. *Science* **377**, 535-539,
633   doi:10.1126/science.abo4628 (2022).
634   22   Gong, X., Renegar, N., Levi, R. & Strano, M. S. Machine learning for the discovery of molecular
635   recognition based on single-walled carbon nanotube corona-phases. *npj Computational Materials* **8**,
636   doi:10.1038/s41524-022-00795-7 (2022).
637   23   Hendler-Neumark, A. & Bisker, G. Fluorescent Single-Walled Carbon Nanotubes for Protein Detection.
638   *Sensors* **19**, 5403, doi:10.3390/s19245403 (2019).
639   24   Kelich, P. *et al.* Discovery of DNA–Carbon Nanotube Sensors for Serotonin with Machine Learning and
640   Near-infrared Fluorescence Spectroscopy. *ACS Nano* **16**, 736-745, doi:10.1021/acsnano.1c08271 (2022).
641   25   Kelich, P. *et al.* Predicting Serotonin Detection with DNA-Carbon Nanotube Sensors across Multiple
642   Spectral Wavelengths. *Journal of Chemical Information and Modeling* **64**, 3992-4001,
643   doi:10.1021/acs.jcim.4c00021 (2024).
644   26   An, S. *et al.* Directed Evolution of Near-Infrared Serotonin Nanosensors with Machine Learning-Based
645   Screening. *Nanomaterials* **14**, 247, doi:10.3390/nano14030247 (2024).
646   27   Beyene, A. G. *et al.* Imaging striatal dopamine release using a nongenetically encoded near infrared
647   fluorescent catecholamine nanosensor. *Science Advances* **5**, eaaw3108, doi:10.1126/sciadv.aaw3108
648   (2019).
649   28   Bulumulla, C. *et al.* Visualizing Synaptic Dopamine Efflux with a 2D Composite Nanofilm. *eLife* **11**,
650   doi:10.7554/ELIFE.78773 (2022).
651   29   Kruss, S. *et al.* High-resolution imaging of cellular dopamine efflux using a fluorescent nanosensor array.
652   *Proceedings of the National Academy of Sciences of the United States of America* **114**, 1789-1794,
653   doi:10.1073/PNAS.1613541114 (2017).
654   30   Elizarova, S. *et al.* A fluorescent nanosensor paint detects dopamine release at axonal varicosities with high
655   spatiotemporal resolution. *Proceedings of the National Academy of Sciences of the United States of*
656   *America* **119**, e2202842119-e2202842119, doi:10.1073/PNAS.2202842119 (2022).
657   31   Kilian, P., Knight, F. R. & Woollins, J. D. Synthesis of ligands based on naphthalene peri-substituted by
658   Group 15 and 16 elements and their coordination chemistry. *Coordination Chemistry Reviews* **255**, 1387-
659   1413, doi:10.1016/j.ccr.2011.01.015 (2011).
660   32   Pelizzetti, E. & Mentasti, E. Kinetics and Mechanism of Oxidation of Catechols by Tris(1,10-
661   Phenanthroline) Iron (III) and Its Derivatives in Aqueous Acidic Perchlorate Media. *Zeitschrift für*
662   *Physikalische Chemie* **105**, 21-34, doi:10.1524/zpch.1977.105.1_2.021 (1977).

663 33 Bergquist, J., Ściubisz, A., Kaczor, A. & Silberring, J. Catecholamines and methods for their identification
664   and quantitation in biological tissues and fluids. *Journal of Neuroscience Methods* **113**, 1-13,
665   doi:10.1016/s0165-0270(01)00502-7 (2002).
666 34 Tsunoda, M. Recent advances in methods for the analysis of catecholamines and their metabolites.
667   *Analytical and Bioanalytical Chemistry* **386**, 506-514, doi:10.1007/s00216-006-0675-z (2006).
668 35 Ribeiro, J. A., Fernandes, P. M. V., Pereira, C. M. & Silva, F. Electrochemical sensors and biosensors for
669   determination of catecholamine neurotransmitters: A review. *Talanta* **160**, 653-679,
670   doi:10.1016/j.talanta.2016.06.066 (2016).
671 36 Barone, P. W., Baik, S., Heller, D. A. & Strano, M. S. Near-infrared optical sensors based on single-walled
672   carbon nanotubes. *Nature Materials* **4**, 86-92, doi:10.1038/nmat1276 (2005).
673 37 Kim, J. H. *et al.* The rational design of nitric oxide selectivity in single-walled carbon nanotube near-
674   infrared fluorescence sensors for biological detection. *Nature Chemistry 2009 1:6* **1**, 473-481,
675   doi:10.1038/nchem.332 (2009).
676 38 Satishkumar, B. C. *et al.* Reversible fluorescence quenching in carbon nanotubes for biomolecular sensing.
677   *Nature Nanotechnology 2007 2:9* **2**, 560-564, doi:10.1038/nnano.2007.261 (2007).
678 39 Yamabe, S., Minato, T. & Kimura, M. Theoretical interpretation of the standard redox potential of
679   benzene-1,2-diol and its derivatives. *The Journal of Physical Chemistry* **85**, 3510-3513,
680   doi:10.1021/j150623a029 (1981).
681 40 Jaramillo, A. M., Barrera-Gutiérrez, R. & Cortés, M. T. Synthesis, Follow-Up, and Characterization of
682   Polydopamine-like Coatings Departing from Micromolar Dopamine-*o*-Quinone Precursor
683   Concentrations. *ACS Omega* **5**, 15016-15027, doi:10.1021/acsomega.0c00676 (2020).
684 41 Zhang, Z. *et al.* Iron Magnetic Nanoparticle-Induced ROS Generation from Catechol-Containing Microgel
685   for Environmental and Biomedical Applications. *ACS Applied Materials & Interfaces* **12**, 21210-
686   21220, doi:10.1021/acsami.9b19726 (2020).
687 42 O'Connell, M. J. *et al.* Band Gap Fluorescence from Individual Single-Walled Carbon Nanotubes. *Science*
688   **297**, 593-596, doi:10.1126/science.1072631 (2002).
689 43 Duque, J. G. *et al.* Stable Luminescence from Individual Carbon Nanotubes in Acidic, Basic, and
690   Biological Environments. *Journal of the American Chemical Society* **130**, 2626-2633,
691   doi:10.1021/ja0777234 (2008).
692 44 Chemicalize , https://chemicalize.com/ (ChemAxon, 2023-2024).
693 45 Silvera-Batista, C. A., Wang, R. K., Weinberg, P. & Ziegler, K. J. Solvatochromic shifts of single-walled
694   carbon nanotubes in nonpolar microenvironments. *Physical Chemistry Chemical Physics* **12**, 6990,
695   doi:10.1039/b927053a (2010).
696 46 Song, C., Pehrsson, P. E. & Zhao, W. Recoverable Solution Reaction of HiPco Carbon Nanotubes with
697   Hydrogen Peroxide. *The Journal of Physical Chemistry B* **109**, 21634-21639, doi:10.1021/jp053077o
698   (2005).
699 47 Jena, P. V. *et al.* A Carbon Nanotube Optical Reporter Maps Endolysosomal Lipid Flux. *ACS Nano* **11**,
700   10689-10703, doi:10.1021/ACSNANO.7B04743 (2017).
701 48 Budhathoki-Uprety, J. *et al.* Synthetic molecular recognition nanosensor paint for microalbuminuria.
702   *Nature Communications 2019 10:1* **10**, 1-9, doi:10.1038/s41467-019-11583-1 (2019).
703 49 Bisker, G. *et al.* Protein-targeted corona phase molecular recognition. *Nature Communications 2016 7:1* **7**,
704   1-14, doi:10.1038/ncomms10241 (2016).
705 50 Gerstman, E., Hendler-Neumark, A., Wulf, V. & Bisker, G. Monitoring the Formation of Fibrin Clots as
706   Part of the Coagulation Cascade Using Fluorescent Single-Walled Carbon Nanotubes. *ACS Applied*
707   *Materials and Interfaces* **15**, 21866-21876, doi:10.1021/ACSAMI.3C00828 (2023).
708 51 Williams, R. M. *et al.* Noninvasive ovarian cancer biomarker detection via an optical nanosensor implant.
709   *Science Advances* **4**, doi:10.1126/SCIADV.AAQ1090 (2018).
710 52 Antman-Passig, M. *et al.* Optical Nanosensor for Intracellular and Intracranial Detection of Amyloid-Beta.
711   *ACS Nano* **16**, 7269-7283, doi:10.1021/acsnano.2c00054 (2022).
712 53 Pinals, R. L. *et al.* Rapid SARS-CoV-2 Spike Protein Detection by Carbon Nanotube-Based Near-Infrared
713   Nanosensors. *Nano Letters* **21**, 2272-2280, doi:10.1021/ACS.NANOLETT.1C00118 (2021).
714 54 Nißler, R. *et al.* Remote near infrared identification of pathogens with multiplexed nanosensors. *Nature*
715   *Communications* **11**, doi:10.1038/s41467-020-19718-5 (2020).

716   55   Chang, C. J., James, T. D., New, E. J. & Tang, B. Z. Activity-Based Sensing: Achieving Chemical
717   Selectivity through Chemical Reactivity. *Accounts of Chemical Research* **53**, 1-1,
718   doi:10.1021/acs.accounts.9b00542 (2020).
719   56   Messina, M. S., Quargnali, G. & Chang, C. J. Activity-Based Sensing for Chemistry-Enabled Biology:
720   Illuminating Principles, Probes, and Prospects for Boronate Reagents for Studying Hydrogen Peroxide.
721   *ACS Bio & Med Chem Au* **2**, 548-564, doi:10.1021/acsbiomedchemau.2c00052 (2022).
722   57   Wheeler, S. E. Understanding Substituent Effects in Noncovalent Interactions Involving Aromatic Rings.
723   *Accounts of Chemical Research* **46**, 1029-1038, doi:10.1021/ar300109n (2013).
724   58   GaussView v. 6.1.1 (Semichem Inc., Shawnee Mission, KS, 2019).
725   59   Hart, K. *et al.* Optimization of the CHARMM Additive Force Field for DNA: Improved Treatment of the
726   BI/BII Conformational Equilibrium. *Journal of Chemical Theory and Computation* **8**, 348-362,
727   doi:10.1021/ct200723y (2012).
728   60   Huang, J. & Mackerell, A. D. CHARMM36 all-atom additive protein force field: Validation based on
729   comparison to NMR data. *Journal of Computational Chemistry* **34**, 2135-2145, doi:10.1002/jcc.23354
730   (2013).
731   61   Zheng, Y., Alizadehmojarad, A. A., Bachilo, S. M., Kolomeisky, A. B. & Weisman, R. B. Dye Quenching
732   of Carbon Nanotube Fluorescence Reveals Structure-Selective Coating Coverage. *ACS Nano* **14**, 12148-
733   12158, doi:10.1021/acsnano.0c05720 (2020).
734   62   Alizadehmojarad, A. A., Bachilo, S. M. & Weisman, R. B. Compositional Analysis of ssDNA-Coated
735   Single-Wall Carbon Nanotubes through UV Absorption Spectroscopy. *Nano Letters* **22**, 8203-8209,
736   doi:10.1021/acs.nanolett.2c02850 (2022).
737   63   Alizadehmojarad, A. A. *et al.* Binding Affinity and Conformational Preferences Influence Kinetic Stability
738   of Short Oligonucleotides on Carbon Nanotubes. *Advanced Materials Interfaces* **7**, 2000353,
739   doi:10.1002/admi.202000353 (2020).
740   64   Nißler, R. *et al.* Quantification of the Number of Adsorbed DNA Molecules on Single-Walled Carbon
741   Nanotubes. *The Journal of Physical Chemistry C* **123**, 4837-4847, doi:10.1021/acs.jpcc.8b11058 (2019).
742   65   Vanommeslaeghe, K. *et al.* CHARMM general force field: A force field for drug-like molecules
743   compatible with the CHARMM all-atom additive biological force fields. *Journal of Computational
744   Chemistry* **31**, 671-690, doi:10.1002/jcc.21367 (2010).
745   66   Phillips, J. C. *et al.* Scalable molecular dynamics on CPU and GPU architectures with NAMD. *The Journal
746   of Chemical Physics* **153**, 044130, doi:10.1063/5.0014475 (2020).
747   67   Darden, T., York, D. & Pedersen, L. Particle mesh Ewald: An N·log(N) method for Ewald
748   sums in large systems. *The Journal of Chemical Physics* **98**, 10089-10092, doi:10.1063/1.464397 (1993).
749   68   Sánchez, H. R. Residence Times from Molecular Dynamics Simulations. *The Journal of Physical
750   Chemistry B* **126**, 8804-8812, doi:10.1021/acs.jpcb.2c03756 (2022).
751   69   Bernetti, M., Masetti, M., Rocchia, W. & Cavalli, A. Kinetics of Drug Binding and Residence Time.
752   *Annual Review of Physical Chemistry* **70**, 143-171, doi:10.1146/annurev-physchem-042018-052340
753   (2019).
754   70   Pan, A. C., Xu, H., Palpant, T. & Shaw, D. E. Quantitative Characterization of the Binding and Unbinding
755   of Millimolar Drug Fragments with Molecular Dynamics Simulations. *Journal of Chemical Theory and
756   Computation* **13**, 3372-3377, doi:10.1021/acs.jctc.7b00172 (2017).

757

758

Acknowledgments

763

Supplementary Materials:

765

Supplementary Materials for

Molecular Determinants of Optical Modulation in ssDNA-Carbon Nanotube Biosensors: Insights from Experimental and Computational Approaches

Andrew T. Krasley[1, †], Sayantani Chakraborty[2, †], Lela Vuković[2,3,*], Abraham G. Beyene[1,*]

[1] Janelia Research Campus, Howard Hughes Medical Institute, Ashburn, VA 20147

[2] Department of Chemistry and Biochemistry, University of Texas at El Paso, El Paso, TX 79968

[3] Computational Science Program and Bioinformatics Program, University of Texas at El Paso, El Paso, TX 79968

* Corresponding authors. Email: lvukovic@utep.edu; beyenea@janelia.hhmi.org

† These authors contributed equally to this work.

Materials and Methods

Experimental Materials and Methods

(GT)₆-SWCNT sensor preparation

HiPCo raw SWCNT (NanoIntegris) were hydrated with H_2O (Milli-Q, 18.2 Ω, 1 g / 50 mL) and stored sealed at room temperature until use. Desalted $(GT)_6$ ssDNA (IDT) was dissolved in 0.1 M NaCl (1 mg / 60 µL) and frozen at -20°C until use. Hydrated SWCNTs (4-5 mg) were combined with $(GT)_6$ (1 mg) and 0.1 M NaCl (1 mL / mg ssDNA) in a 12 x 75 x 1 mm glass culture tube and bath sonicated (Branson 1800) for 20 min on high at room temperature. Contents were then transferred to a microwave tube

21

796 (Biotage conical 0.5-2.0 mL, Part No. 352016) and probe sonicated (Sonics Vibracell VCX 230, ¼"
797 probe, 50% amplitude, centered and tip at 15 mm from bottom of tube) for 15 min in an ice bath. After,
798 the contents were transferred to a 1.5 mL microcentrifuge tube and centrifuged in a fixed angle rotor at
799 20,000 rcf, for 1 h, at 4°C. The supernatant was transferred to a new 1.5 mL centrifuge tube and the pellet
800 was discarded. The suspension was then re-centrifuged for an additional hour at 20,000 rcf, 4°C, in the
801 same rotor. The supernatant was then removed, and 2nd pellet discarded. To account for possible
802 differences in preparation, multiple 1 mL preparations were run this way and combined to create one bulk
803 solution (10 preparations total). An aliquot of this bulk supernatant was diluted (10X) and absorbance
804 measured at 632 nm (NanoDrop One C) was used to estimate stock concentrations. The bulk supernatant
805 solution was diluted to 100 ppm with 0.1M NaCl and stored at 2-8°C until use.

806 *Analyte stock preparation*

807 All analytes were made from commercially available vendors and used without further purification.
808 Please see Table S5 for a list of compounds, sources, and calculated values. All analytes were freshly
809 made into 10 µM stocks in dimethyl sulfoxide (DMSO, spectrophotometric grade), aliquoted into argon
810 filled amber 1.5 mL tubes, topped with argon again, and frozen at -20°C for up to three months. For use in
811 assay, samples were thawed and diluted to 1 µM working concentrations with DMSO.

812 *pH measurements*

813 All pH measurements were taken with an Orion Star A111 pH meter using an Orion PerpHecT ROSS
814 Combination pH Micro Electrode capable of measurements in a 96-well plate. All measurements were
815 taken after the probe was freshly calibrated using 4.01, 7.00, and 10.01 standards. pH measurements were
816 taken of pH-adjusted 10 ppm $(GT)_6$-SWCNT prior to aliquoting into plate wells. This measurement had to
817 remain unchanged (± 0.05 pH units) for 1 h to ensure equilibrium had been reached prior to aliquoting.
818 After substrates were added and all measurements taken, the pH of individual wells were then measured.
819 The average values of the three well used for each analyte were used as the average pH and response for
820 the respective compound. The measurements were typically taken between 65 min and 90 min after the
821 analyte was initially added to the 10 ppm solution.

822 *Plate reader solution-phase fluorescence measurements*

823 All readings were taken on a custom built 96-well plate reader. All readings were taken with 10 ppm
824 $(GT)_6$-SWCNT in 0.1M NaCl (198 µL), n = 3, readings taken with a 658 nm laser, 52.4 mW, 1000 ms
825 exposure, 3 averages, and additives were added in DMSO (2 µL of 1 mM) unless otherwise noted. A well
826 containing 0.1M NaCl (198 µL) and DMSO (2 µL) were used for blank subtraction. Baseline
827 measurements were taken approximately 15 min after the 10 ppm solution was aliquoted. Substrates were
828 added to all wells, and measurements were taken at 4 min, 8 min, 15 min, 30 min, 45 min, and 60 min
829 after addition to the last well. This study used the 30 min reading values and the same trends were seen at
830 other time points as well. Periphery wells were not used for measurements and each plate contained
831 dopamine (**DA**) for normalization, pyrogallol (**MM**) as a positive control, and octopamine (**OO**) as a
832 negative control.

833 *ELISA*

834 The dopamine ELISA kit (ImmuSmol SAS, Bordeaux, France) was run experimentally and processed in
835 accordance with the manufacture's guidelines and standard operating procedure. For sample preparation,
836 a 96-well plate was prepared with wells containing 198 µL of 10 ppm (GT)$_6$-SWCNT in 0.1M NaCl that
837 were spiked with DA (10 µM final concentration) or dopaquinone (DQ, 10 µM final concentration) as a
838 substrate in DMSO (2 µL of 1 mM), and 198 µL of 0.1M NaCl containing DA (10 µM final
839 concentration) as a substrate in DMSO (2 µL of 1 mM). For each respective substrate run, one well was
840 exposed to 104.8 mW of 658 nm laser for 1 h and the other was exposed no laser, with mixing via pipette
841 aspiration every 15 min. After 1 h, the contents of each well were filtered through a 100 kDa molecular
842 weight cutoff (MWCO) centrifuge cartridge to remove SWCNT, and the filtrate collected. 28.2 µL of
843 filtrate was combined with 235 µL of ethylenediaminetetraacetic acid (EDTA, 10 mM), 235 µL of sodium
844 metabisulfite (40 mM) and 1851.8 µL of water, before being frozen at -80°C. Dilution was necessary for
845 sample to fit within the kits dynamic range, and EDTA and sodium metabisulfite were added to prevent
846 dopamine degradation as per the manufacturers protocol. Samples were then thawed to room temperature
847 and run in a quantitative DA ELISA kit following the manufacturers protocol. Standards and samples
848 were run as n = 3 and quality control (QC) samples as n = 2. The ELISA plates were read using a Tecan
849 Spark microplate reader at 450 nm with 625 nm reference. Data was then processed using Graphpad
850 Prism 10. Standards were treated with four parameter logistic regression as per the manufacturers protocol
851 and the QCs, exposed, and unexposed samples were interpolated from this curve.

852 *pK$_A$ modleing*

853 pK$_A$ modeling and chemoinformatic values were generated using Chemicalize software from ChemAxon.
854 Values were computed between March 2023 and April 2024.[44]

855 *HPLC*

856 Aqueous solutions of DA (40 mM) and NaIO$_4$ (35 mM) were prepared. A 500 µL aliquot of the DA
857 solution was combined with a 500 µL aliquot of NaIO$_4$, and the solution was vortexed and kept at room
858 temperature for 10 min before an aliquot was taken for HPLC analysis. A 500 µL aliquot of DA (40 mM)
859 was diluted with 500 µL of H$_2$O to produce a 20 mM solution of DA. Two wells on opposite sides of a 96
860 well plate (e.g., C2 and C11) were loaded with 10 ppm (GT)$_6$-SWCNT in H$_2$O (198 µL) and 2 µL of the
861 20 mM DA solution was added to each. One well was exposed to a 658 nm laser (104.8 mW) and one was
862 not. The wells were agitated with a pipette every 15 min for 1 h total. After, the contents of the wells were
863 filtered through 100 kDa MWCO centrifuge filters (15,000 rcf, 4°C, 2 min, fixed angle rotor) to remove
864 the SWCNT and the filtrate was taken for analysis by HPLC. Please refer to supplementary information
865 for HPLC runs and conditions.

866 **Computational Materials and Methods**

867 *Atomistic models of (GT)$_6$-(9,4)-SWCNT systems with analyte molecules*

868 The initial configuration of (9,4)-SWCNT wrapped with three (GT)$_6$ chains was taken from
869 previously reported results.[12] The small molecules were built with GaussView software.[58] We use our
870 own tcl script for making six replicas of each analyte and for combining them with the (GT)$_6$-SWCNT
871 system. All the (GT)$_6$-SWCNT systems with six analyte molecules were solvated and neutralized in 0.1 M
872 NaCl aqueous solution with TIP3P water model, using *solvate* and *ionize* VMD plugins, respectively.
873 Total number of atoms in each of these systems are listed in

23

874   Table S4.

Classical molecular dynamics simulations

876   Atomistic simulations were performed with each of the prepared systems to gain an insight in the
877   molecular level behavior of the nanosensor conjugate as it binds to the analyte molecules. The systems
878   were described with CHARMM36 force field parameters[59,60] as they have been successfully used to
879   model interactions between ssDNA molecules and SWCNTs in previous studies.[12,61-64] The parameters for
880   the analyte compounds were generated from the CGenFF website,[65] based on CHARMM36 general force
881   field parameters. The simulations were performed with NAMD2.13 package[66] using Langevin dynamics
882   in the NpT ensemble, where the value of the Langevin constant γ_{Lang} was set at 1.0 ps^{-1}, the pressure
883   remained constant at 1 bar, and the temperature remained constant at 298 K. The integration time step was
884   set to 2 fs, and Coulomb and van der Waals non-bonded interactions were evaluated every one- and two-
885   time steps, respectively, for all atoms within a 12 Å cutoff distance. The long-range Coulomb interactions
886   were evaluated using the particle-mesh Ewald (PME) method,[67] with periodic boundary conditions
887   applied in all directions. After 5,000 steps of minimization, solvent molecules were equilibrated for 0.1 ns
888   around the ssDNA-SWCNT conjugate. For this purpose, the atoms were restrained using harmonic forces
889   with a spring constant of 1 kcal (mol·Å)$^{-1}$. Next, the systems were equilibrated in production MD runs,
890   with harmonic wall restraints applied on the ssDNA side chains (A and C) and the small molecules. For
891   the harmonic wall restraints, upper and lower walls were defined at 19 and -19 Å, respectively and a
892   spring constant of 10 kcal (mol·Å)$^{-1}$ was applied. The lengths of all simulations are listed in Table S4.

Contact area calculations

894   Contact areas between two selections of atoms A and B (e.g., analyte molecules, ssDNA
895   nucleotides, SWCNT surface, etc.) at time *t*, $s_{contact\ area}(t)$, were calculated for the whole MD
896   trajectories (~6 μs) based on the following equation:

897    $$s_{contact\ area}(t) = \frac{s_A(t) + s_B(t) - s_{AB}(t)}{2} \qquad (1)$$

898   where $s_A(t)$ and $s_B(t)$ are the solvent accessible surface areas (SASA) of atoms within selections A and B
899   at time t, respectively. $s_{AB}(t)$ represents SASA of both selections A and B altogether. The contact areas
900   were calculated with the SASA VMD plugin, where the van der Waals radius of atoms was defined as 1.4
901   Å to designate the points on a sphere which are accessible to the solvent.

Distance calculations

903   To quantify the binding modes visually observed from the MD trajectories and also to analyze the
904   effect of the polar groups, we calculated distances between the centers of mass of selected parts of the
905   analyte molecules (aryl ring, polar groups) and the SWCNT surface at time *t*:

906    $$d(t) = r_{analyte}(t) - r_{SWNT} \qquad (2)$$

907   where $r_{analyte}(t)$ is the radial distance of the center of mass of the selected analyte atoms at time *t*,
908   defined in the cylindrical coordinate system, and r_{SWNT} is the radius of the (9,4)-SWCNT.

Calculation of the percentage of binding time for analytes binding to the SWCNT surface or ssDNA-SWCNT corona

24

Here, we are quantifying the percentage of time in a total trajectory for which the analyte molecules are bound to the sensor conjugate. From the contact area calculations, we imposed a condition to exclude the frames where the analyte molecules are not binding to either the ssDNA-SWCNT corona or the SWCNT surface and are somewhere in the water box. We concurred that if the analyte molecules were far away from the ssDNA-SWCNT conjugate in the water box the contact area with ssDNA-SWCNT/SWCNT would be near 0, so we excluded all those frames and counted only the number of times the contact areas were greater than 1, which signified that the analyte molecules were in the proximity of the ssDNA-SWCNT conjugate. Ultimately, we divided the count of times the analytes molecules were bound to the nanosensor conjugate by the total number of frames to get the percentage of binding time for each molecule of each analyte type.

Residence time calculations for binding to SWCNT surface or ssDNA-SWCNT corona

Residence time (τ_R) for an analyte binding to a specific target is defined as the time it remains in a specific contact position with its target.[68,69] Mathematically, it is inverse of the dissociation rate (k_{off}) of the analyte-target complex. k_{off} is the inverse of the average of time the analyte molecules are bound to the target in different binding events (t_{off}).[70] So, in turn, residence time becomes equivalent to t_{off}.

$$\tau_R = \frac{1}{k_{off}} \; ; k_{off} = \frac{1}{t_{off}}$$

$$\tau_R = t_{off}$$

$$t_{off} = \frac{\sum(t_i \times n_i)}{\sum n_j} \qquad (3)$$

In equation (3), t_i is the duration of a binding event of certain duration i, and n_i is the total number of binding events with duration i. n_j is the number of binding events with different durations (j = $i_1+i_2+i_3+\dots$).

From the contact area calculations, we extracted the frames for which the analyte molecules are binding to the SWCNT surface or the ssDNA-SWCNT conjugate by imposing certain conditions. To qualify as a binding event, the contact area between the analyte molecules and the ssDNA-SWCNT corona or the SWCNT surface must be greater than 30 $\mathring{A}^2$, and for the analyte molecules with amine groups, the distance between the amine groups and the SWCNT surface must be less than 10.5 $\mathring{A}$. The duration of each binding event is then extracted and used to calculate the t_{off} or residence time using equation (3). We used our own Python codes for all these calculations. For each analyte type, all the binding events of all the six molecules were summed up together to calculate the t_{off}.

Supplementary Figures

25

948

949
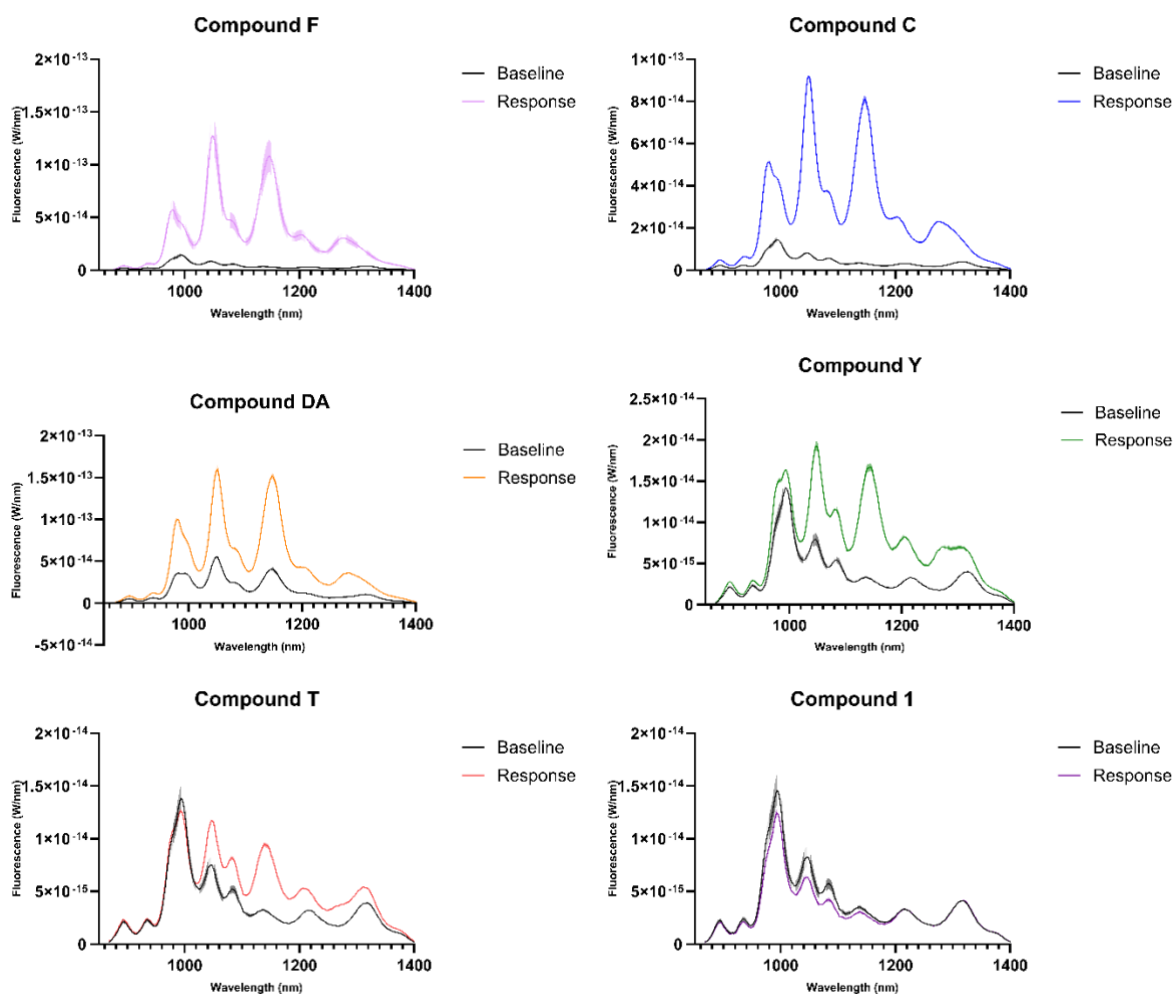
950
951
Fig. S1. Example of baseline and response fluorescence spectra collected for six compounds. Experimental fluorescence
measurements of the $(GT)_6$-SWCNT suspension were taken 30 min after the addition of compounds (10 μM). All readings
were taken with 10 ppm $(GT)_6$-SWCNT in 0.1M NaCl, n = 3, readings taken with a 658 nm laser, 52.4 mW, 1000 ms exposure,
3 averages, and additives were added in DMSO (2 μL of 1 mM). Solid lines are mean with one standard deviation at 50%
transparency in in the same color.
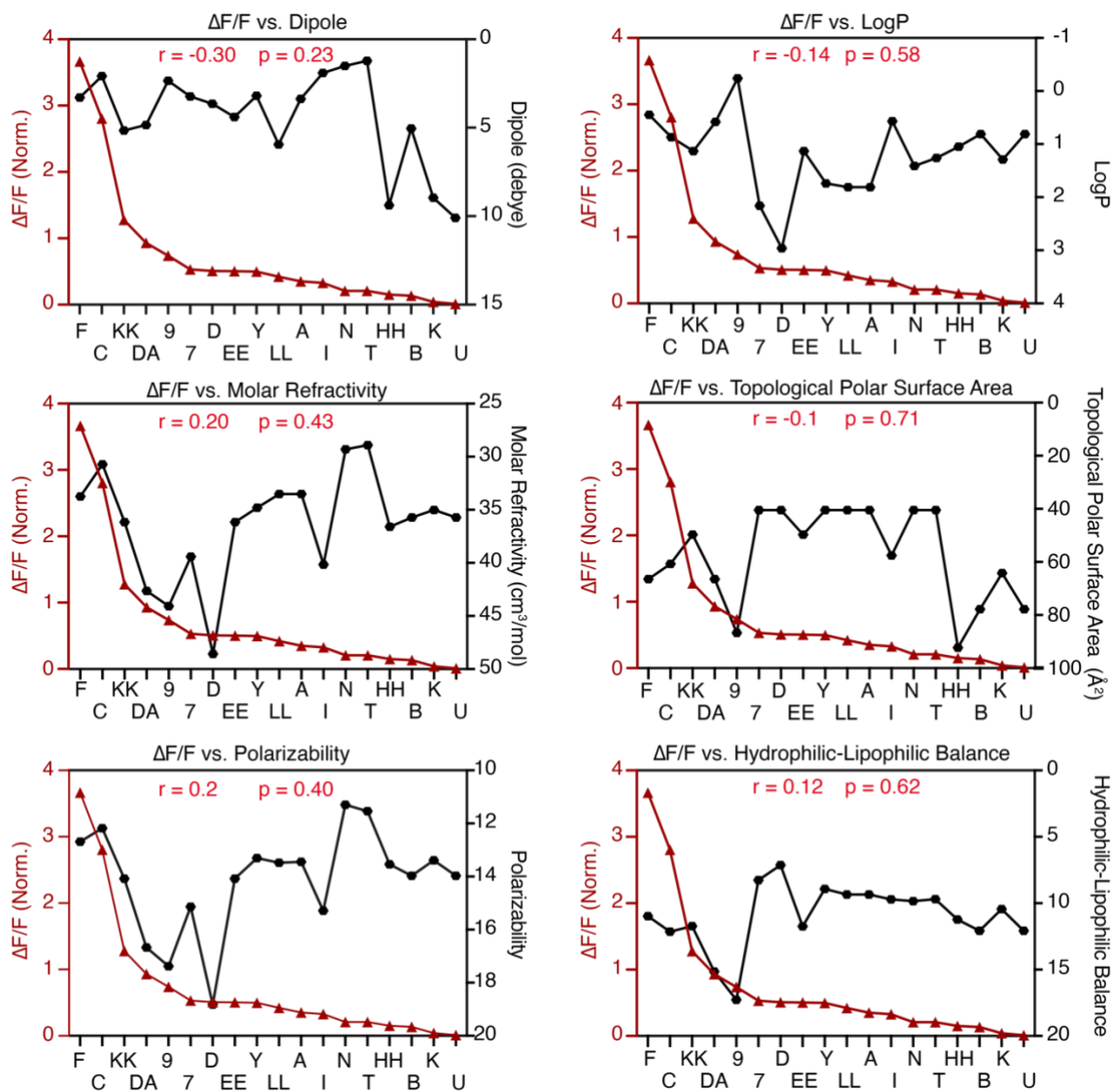
Fig. S2. Comparisons of subset of 18 compounds between experimental and various electronic, physical, and calculated properties. See Fig. 2a for subset of compounds with structures. Experimental ΔF/F (norm., mean) measurements in 0.1M NaCl normalized to dopamine response (dopamine = 1.0 ΔF/F). No correlation was observed among these six. Dipole values were computed using Spartan'20 V1.1.14 on minimized structures using equilibrium geometry at ground state in water with density functional B3LYP 6-31G*. LogP, molar refractivity, and topological polar surface area were calculated using Chemdraw 22.0.0. Polarizability and hydrophilic-lipophilic balance were calculated using Chemazon Chemixalize. Experimental fluorescence measurements of the $(GT)_6$-SWCNT suspension were taken 30 min after the addition of compounds (10 µM). All reading were taken with 10 ppm $(GT)_6$-SWCNT in 0.1M NaCl, n = 3, readings taken with a 658 nm laser, 52.4 mW, 1000 ms exposure, 3 averages, and additives were added in DMSO (2 µL of 1 mM).
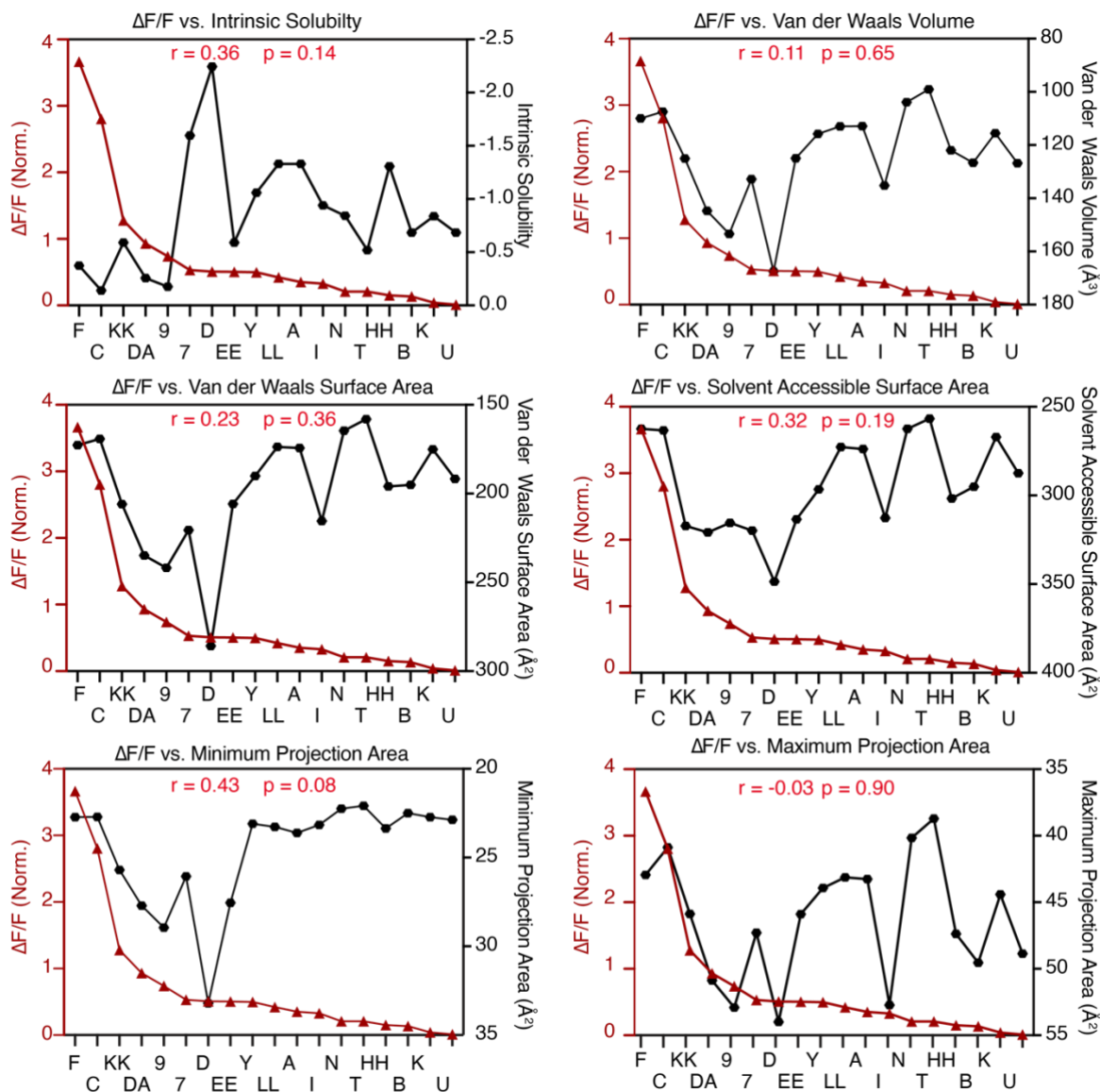
Fig. S3. Comparisons of subset of 18 compounds between experimental and various electronic, physical, and calculated properties. See Fig. 2a for subset of compounds with structures. Experimental $\Delta F/F$ measurements in 0.1M NaCl normalized to dopamine response (dopamine = 1.0 $\Delta F/F$). No correlation was observed among these six. Intrinsic solubility, Van der Waals volume and surface area, solvent accessible surface area, and minimum and maximum projection areas were all calculated using Chemaxon Chemicalize. Experimental fluorescence measurements of the $(GT)_6$-SWCNT suspension were taken 30 min after the addition of compounds (10 µM). All reading were taken with 10 ppm $(GT)_6$-SWCNT in 0.1M NaCl, n = 3, readings taken with a 658 nm laser, 52.4 mW, 1000 ms exposure, 3 averages, and additives were added in DMSO (2 µL of 1 mM).

28
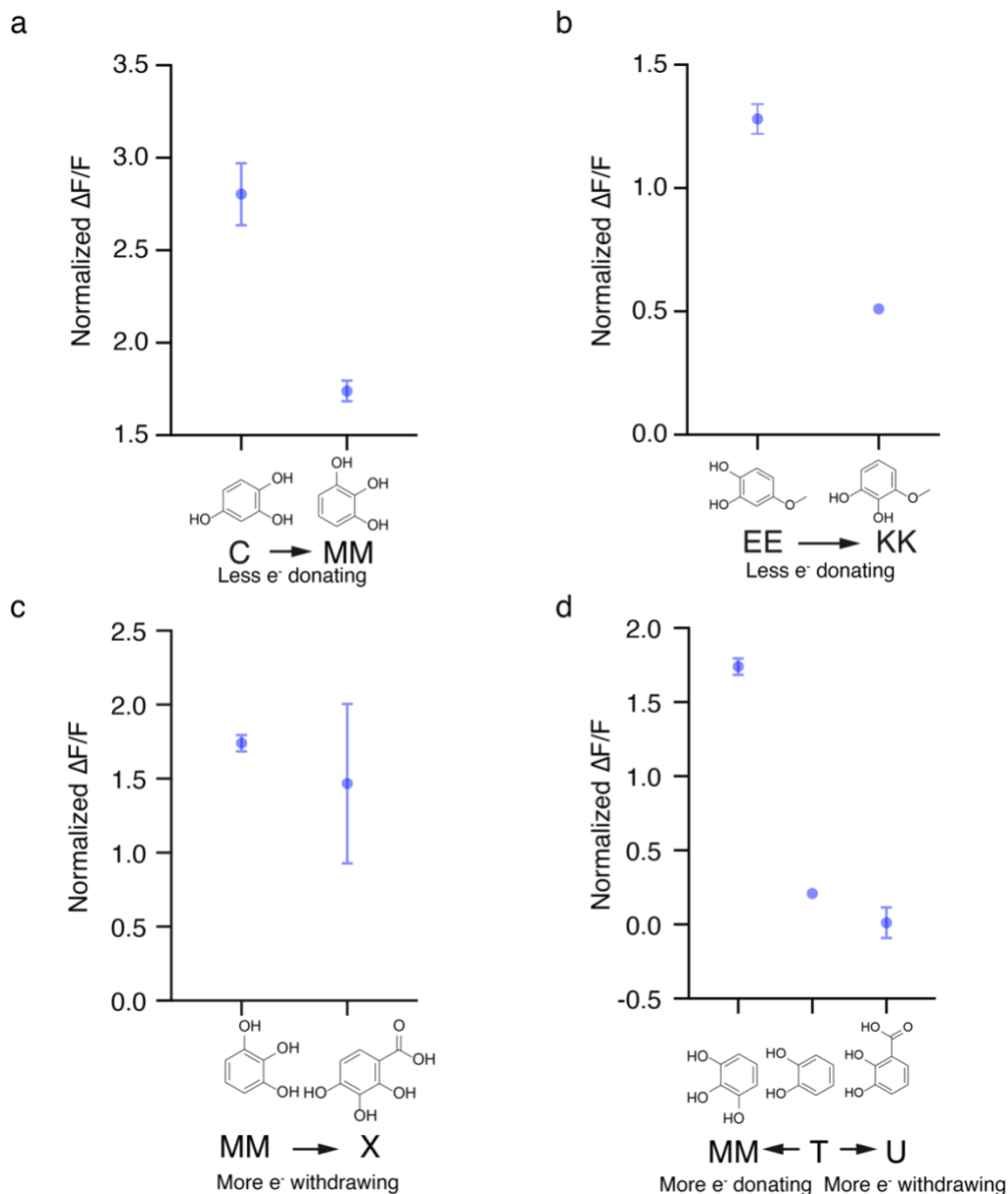
Fig. S4. Comparative analysis of normalized change in fluorescence to electron donating and withdrawing substituents on benzene-1,2-diols. Trends demonstrate that more electron donating substitutes or less electron withdrawing substitutes produce a larger change in fluorescence than their respective less donating or more withdrawing counterparts. Normalization was relative to dopamine = 1.00. **a,** When a hydroxyl is in the 4-position (**C**), it is able to donate more density than when a hydroxyl is in the 3-position (**MM**) and it has a larger change in fluorescence. **b,** In the same manner as (**a**), the methoxy in the 4-position (**KK**) is more electron donating than when in the 3-position (**EE**), leading to a higher change in fluorescence. **c,** When looking at isomers where electron withdrawing groups are added, the compound containing the electron withdrawing group (**X**) produces a lower change in fluorescence than its isomer without the withdrawing group (**MM**). **d,** When applying this concept to benzene-1,2-diols that have a donating group (**MM**) or withdrawing group (**U**) relative to benzene-1,2-diol (**T**) the same trend can be observed, with more donating producing a larger change in fluorescence than the withdrawing substituents.

994
995
996
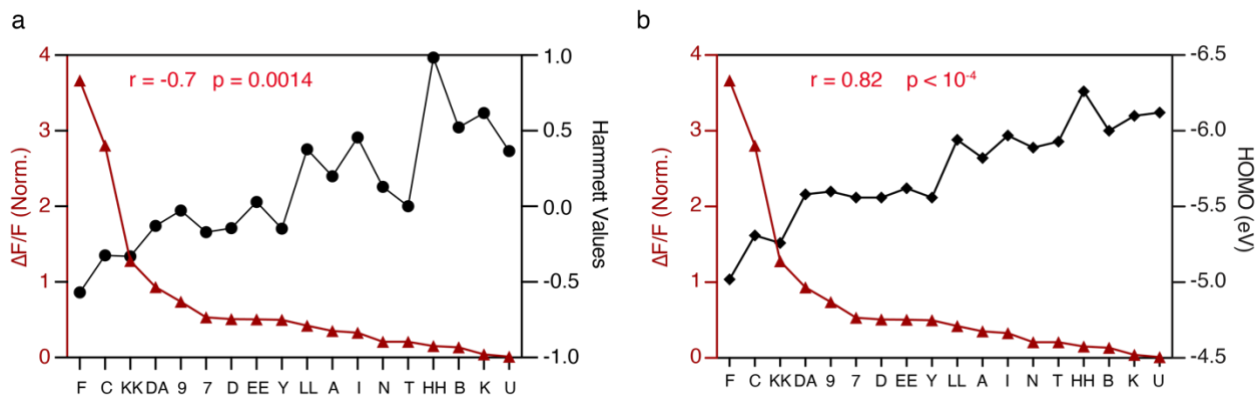
Fig. S5. Correlations between optical modulations and Hammett values or computationally determined e$_{HOMO}$ levels. a,
Correlational analysis of change in fluorescence for each compound (mean, normalized relative to dopamine = 1.00) vs. their
calculated Hammett values showing a positive relationship. This is a complementary presentation of the data presented in Fig.
2C. **b,** Correlational analysis of change in fluorescence for each compound (normalized relative to dopamine = 1.00) vs. their
calculated HOMO level showing a positive relationship. All HOMO values were calculated using Spartan'20 V1.1.14 on
minimized structures using equilibrium geometry at ground state in water with density functional B3LYP 6-31G*.

30
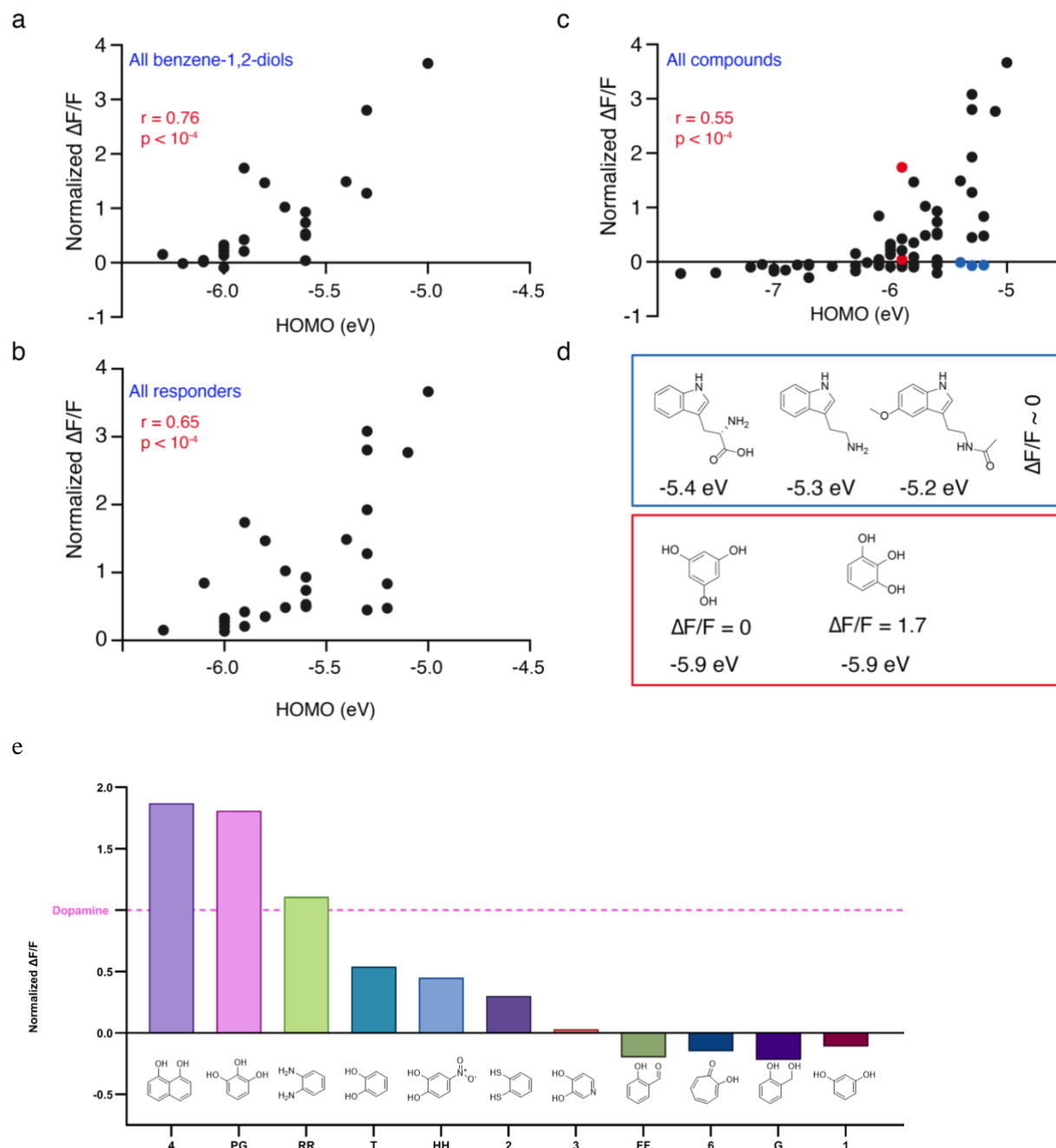
Fig. S6. Correlational analysis of change in fluorescence for each compound vs. their calculated HOMO level. All compounds mean values normalized to dopamine = 1.00. **a,** Analysis of all benzene-1,2-diols showing a positive correlation. **b,** Analysis of all responsive compounds (groups I, II and III in Fig. 1c) showing a positive correlation. **c,** Analysis of all compounds showing a positive correlation. **d,** HOMO level alone is not enough to predict responsiveness, and that vicinal hydrogen bond donors are needed along with needing the system to be conjugated. The colored boxes reflect the respective compounds the in same color in (**c**). **e,** Trend showing that vicinal hydrogen bond donors are needed for a response and that more electron donating rich systems produce a higher response. All HOMO values were calculated using Spartan'20 V1.1.14 on minimized structures using equilibrium geometry at ground state in water with density functional B3LYP 6-31G*.

a

	Acceptance Range (ng/mL)	Sample Value (ng/mL)
QC1	1.8-4.2	4.1
QC2	6.0-14	13

b

c
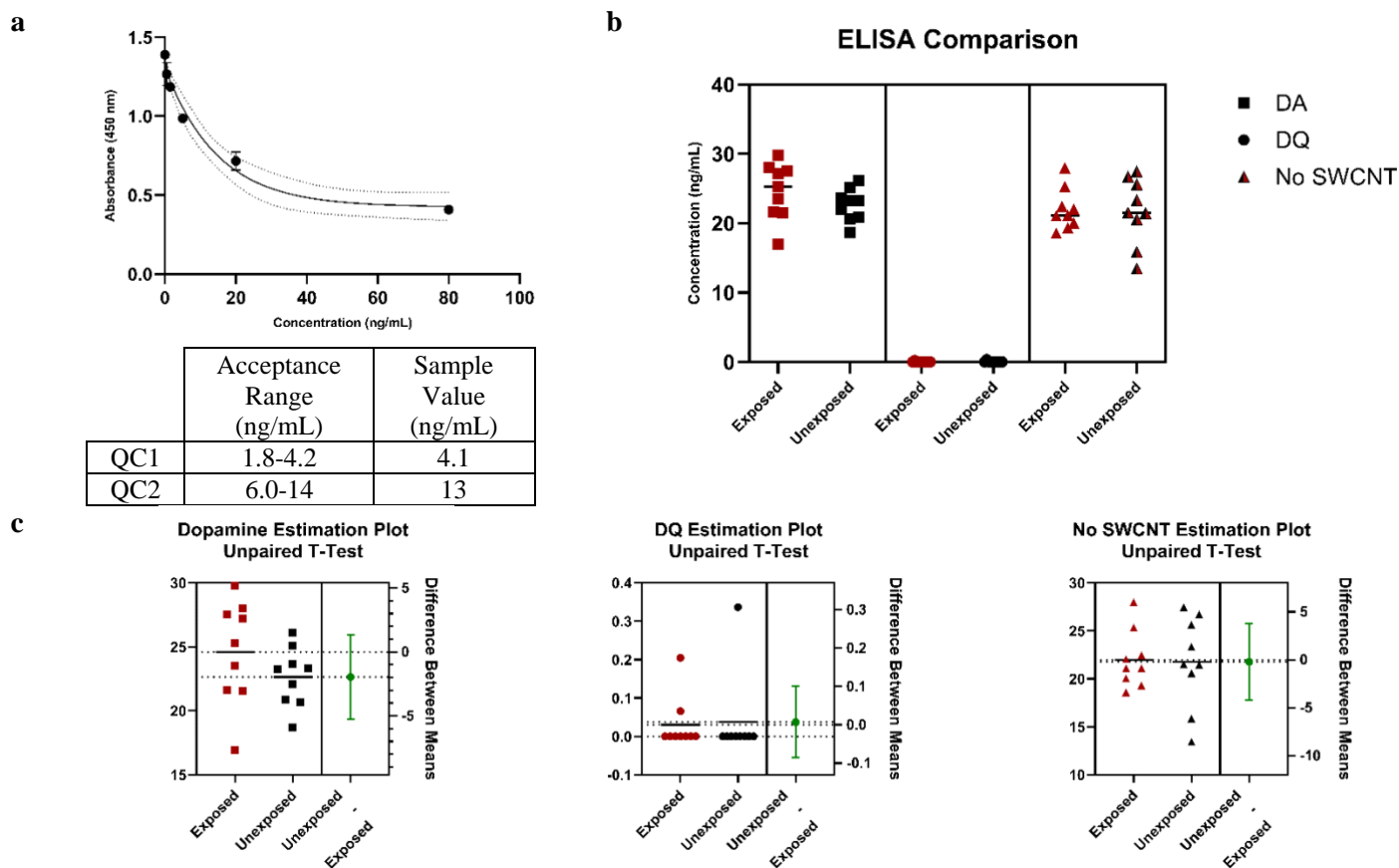
Fig. S7. Dopamine ELISA results showing no difference between samples exposed and unexposed to 658 nm light. This lack of difference between exposed and unexposed samples indicates that the same level of dopamine is present in both. The ELISA kit (ImmuSmol SAS, Bordeaux, France) was run experimentally and processed in accordance with the manufacture's guidelines and standard operating procedure. It has a functional sensitivity of 5 pg/mL and a LOD of 3.3 pg/mL. **a,** Standard curve used for interpolation and QC results. **b,** Comparison of interpolated results. DA = dopamine, DQ = dopaquinone, No SWCNT = samples run without SWCNT present in solution. **c,** Unpaired t-tests showing no significant difference between exposed and unexposed populations of each.

32

1022

1023
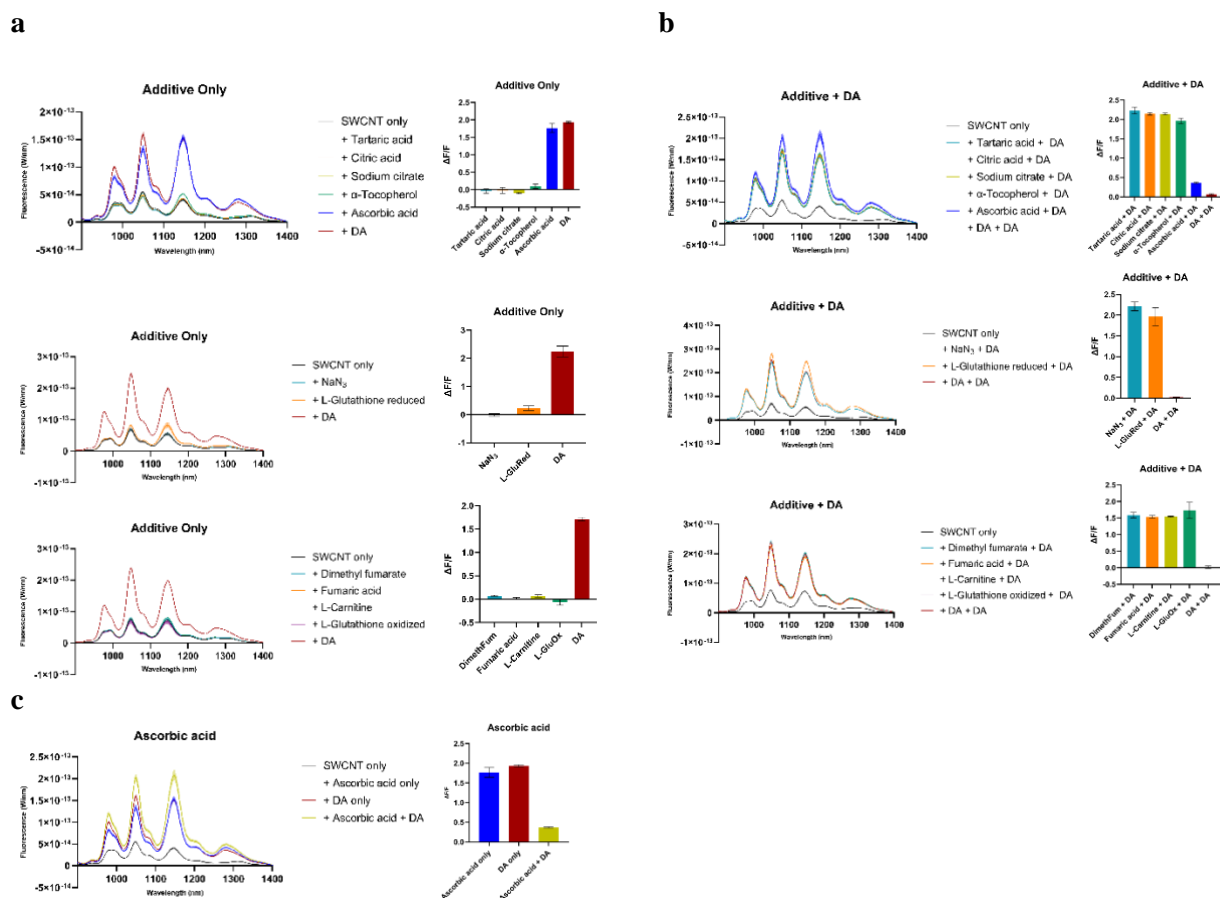
1024 **Fig. S8. The effect of reducing agents and reactive oxygen species scavengers on ΔF/F response to dopamine.** The
1025   addition of antioxidants (10 µM) did not inhibit the response of the $(GT)_6$-SWCNT sensor (10 ppm) to dopamine (10 µM). **a,**
1026   Fluorescence measurements of the $(GT)_6$-SWCNT 6 min after the addition of 10 µM of antioxidant. **b,** Fluorescence
1027   measurements of the $(GT)_6$-SWCNT 15 min after the addition of antioxidant (10 µM) and 6 min after the addition of dopamine
1028   (10 µM). ΔF/F was measured with Additive + DA 6 min being used as the baseline. **c,** Ascorbic acid (10 µM) showing sensor
1029   response, then an increase in response upon the addition of dopamine (10 µM). For ascorbic acid only and DA only, ΔF/F was
1030   measured with SWCNT only as the baseline. For ascorbic acid + DA, ΔF/F was measured with ascorbic acid only as the
1031   baseline. All reading were taken with 10 ppm $(GT)_6$-SWCNT in 0.1M NaCl, n = 3, readings taken with a 658 nm laser, 104.8
1032   mW power, 200 ms exposure, 5 averages, and additives were added in DMSO (2 µL of 1 mM).

1033

1034

1035

1036

1037

1038

1039

1040

1041

1042

1043

C

33
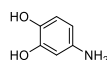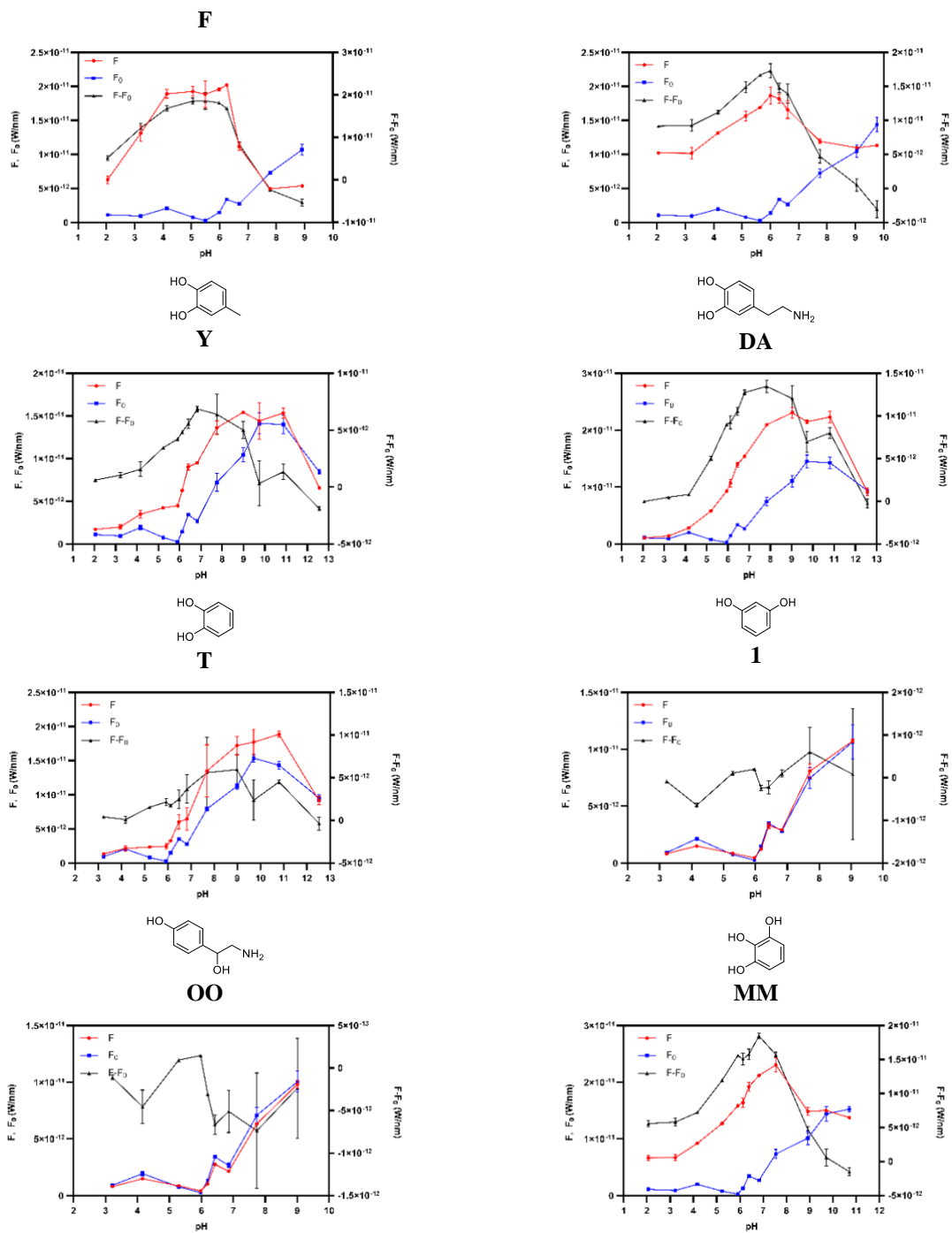
1044

Fig. S9. Eight compounds screened at different pH's from 2-13. Baseline fluorescence (blue, left axis), response fluorescence after addition of analyte (red, left axis), and change in response (black, right axis) for subset of analytes to determine pH effects. All reading were taken with 10 ppm $(GT)_6$-SWCNT in 0.1M NaCl, n = 3, readings taken with a 658 nm laser, 542 mW power, 1000 ms exposure, 3 averages, and additives (10 µM) were added in DMSO (2 µL of 1 mM).
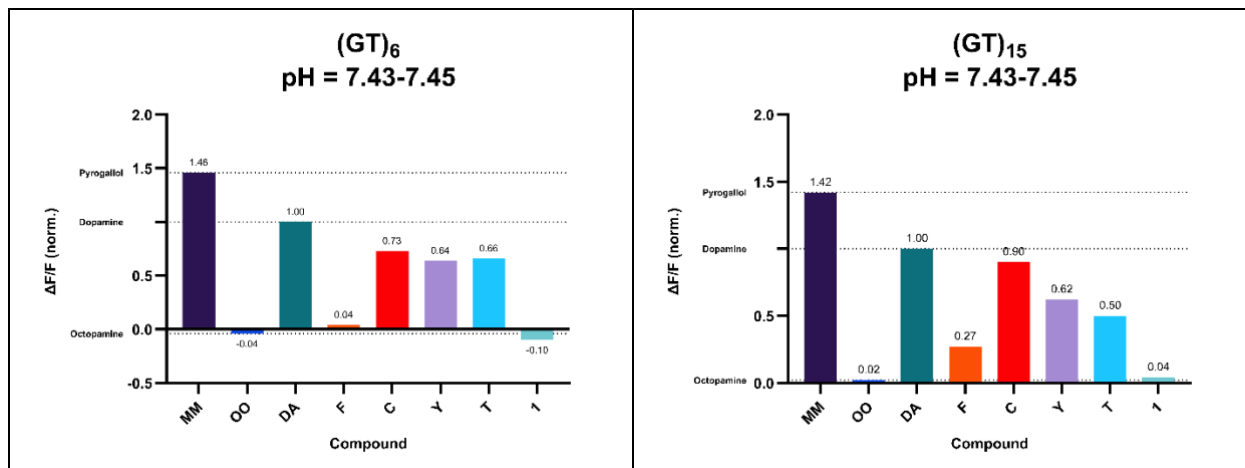
1049

Fig. S10. Comparison of normalized mean ΔF/F for 8 compounds using (GT)$_6$- vs (GT)$_{15}$-SWCNT. The same general
trends can be observed in both ssDNA sequences suggesting that results can be generalized to (GT)$_N$ type systems. All reading
were taken with 10 ppm (GT)$_N$-SWCNT in 1:9 0.1M NaCl:1X PBS, n = 3, readings taken with a 658 nm laser, 542 mW power,
1000 ms exposure, 3 averages, 30 min timepoint after additive addition, and additives (10 µM) were added in DMSO (2 µL of
1 mM). Samples were diluted with 1X PBS to control pH. Normalized to dopamine = 1.00. (GT)$_{15}$ ssDNA (IDT) was
processed in the same manner as (GT)$_6$ (see Methods).

1056
1057
1058
1059

35
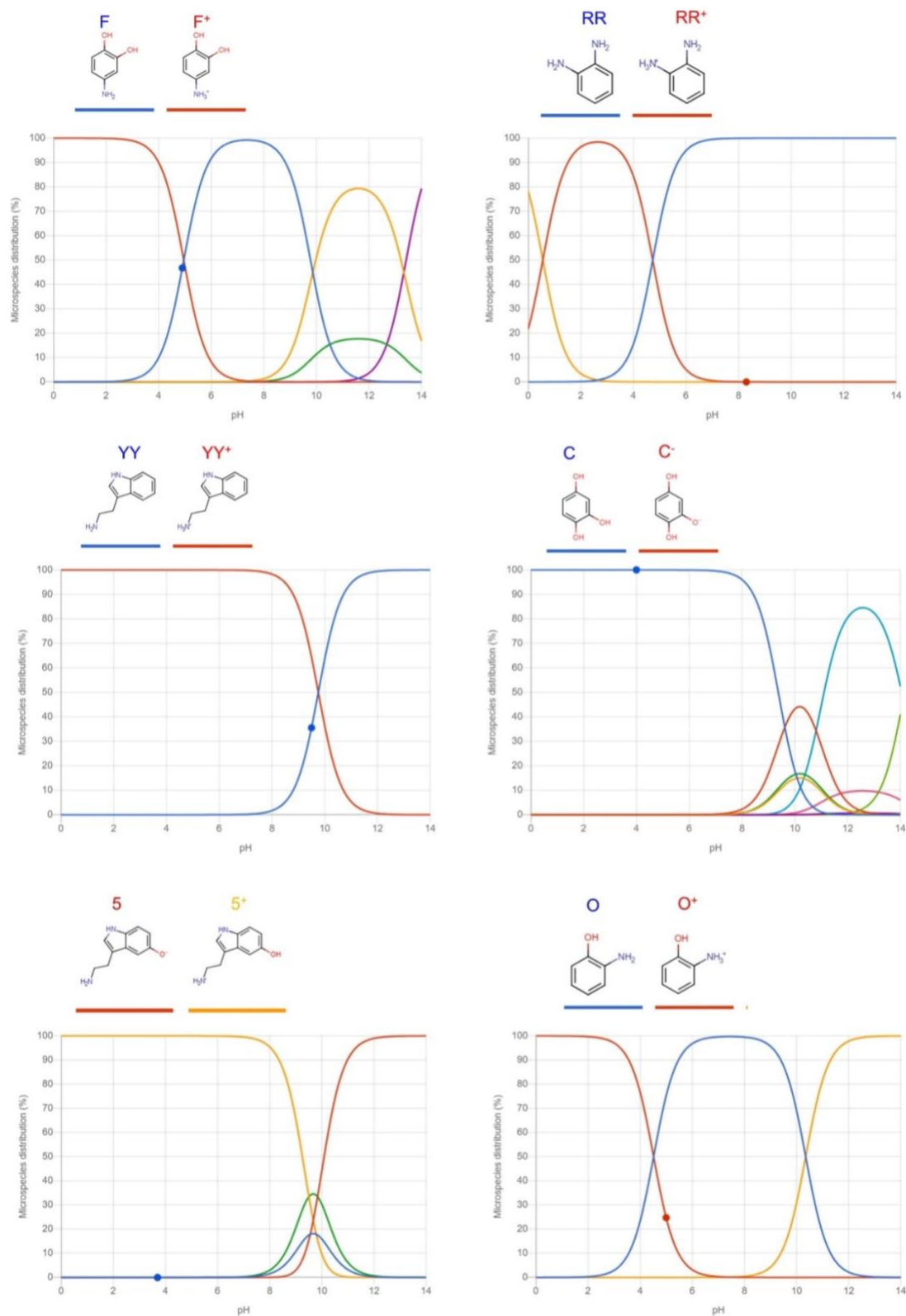
1060
1061 **Fig. S11. Protonation states of modeled molecules F, RR, YY, C, 5 and O at different pHs.** The microspecies vs pH
1062 distribution plots were obtained from Chemaxon Chemicalize. Species not of interest have been omitted.

36
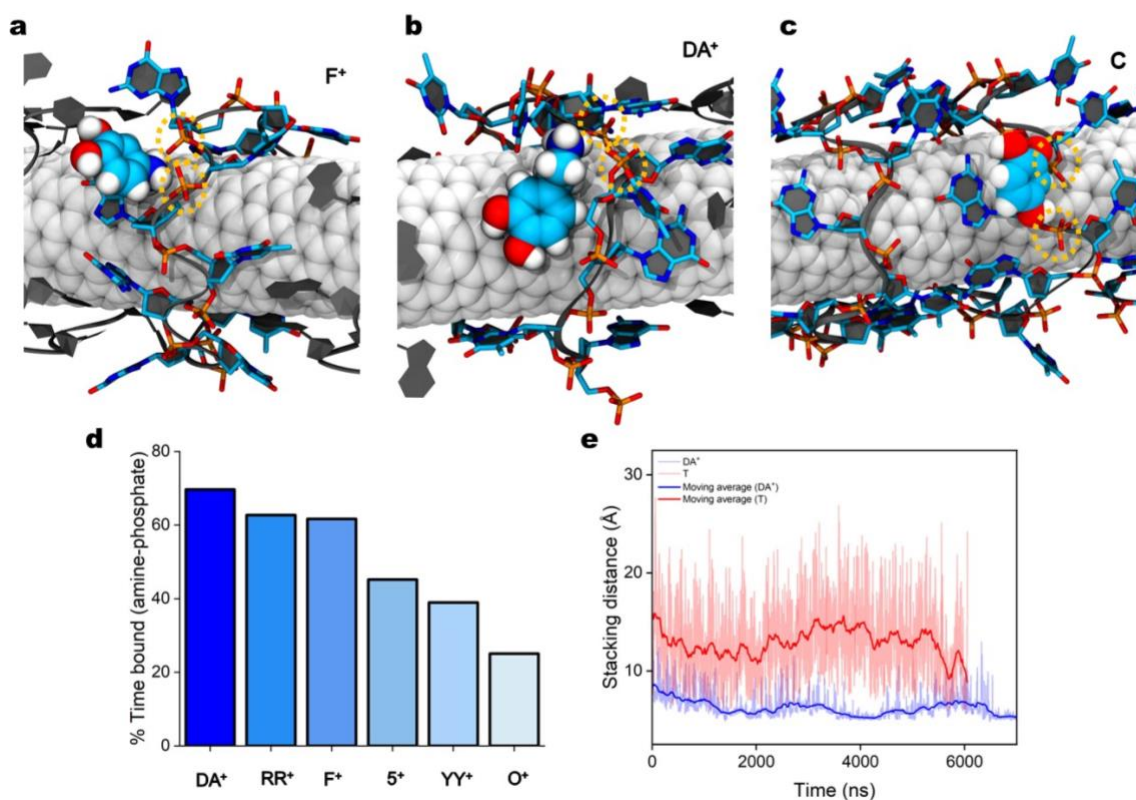
Fig. S12. Binding interactions between positively charged amine groups of analytes and negatively charged DNA phosphate backbone. a, b, The snapshots show the molecules F^+ and DA^+ molecules in their predominant binding modes with their amine groups pointed towards the DNA phosphate backbone atoms. **c,** The C molecules are also shown in their predominant binding modes where the OH groups exhibit repulsive interactions with the DNA phosphate backbone atoms. SWCNT atoms are shown as white spheres, the $(GT)_6$ DNA strands are shown as dark grey ribbons, and the analyte molecules heavy atoms are shown as van der Waals spheres (C: cyan, N: blue, O: red). The orange dotted circles are used to highlight the phosphate groups participating in the interaction. **d,** The plot shows the average percentage of time each of the analyte molecules spend with their amine groups interacting with the phosphate backbone in a decreasing order. Only significant binding events (longer than at least 300 ns) are considered for this calculation. **e,** The plot shows analyte binding in terms of stacking distances for molecules DA^+ and T, over time.

1078   **Fig. S13. HPLC conditions and spectra.**

1079

1080   Solvent A: 95:5 H_2O:ACN + 30 mM Ammonium Formate

1081   Solvent B: 15:85 H_2O:ACN + 30 mM Ammonium Formate

Time (min)	Flow (mL/min)	%A	%B
0.00	2.00	0	100
0.80	2.00	0	100
3.00	2.00	10	90
6.00	2.00	10	90
10.00	2.00	0	100

1082   Sample Temp.: 8°C

1083   Column Temp.: 40°C

1084   Injection Volume: 1.0 µL

1085   Sample Matrix: H_2O

1086   PDA wavelength: 280 nm

1087   HPLC: Waters Arc Premier

1088   Column: 4.6 x 50 mm x 2.5 µm XBridge Premier BEH Amide with VanGuard

38

SAMPLE INFORMATION

Sample Name:	DA	Acquired By:	System
Sample Type:	Unknown	Processing Method	10 min processing
Vial:	1:A,2	Channel Name:	2998 Ch6 280nm@4.8nm
Injection #:	1	Proc. Chnl. Descr.:	2998 Ch6 280nm@4.8nm
Injection Volume:	1.00 ul		
Run Time:	10.0 Minutes		
Date Acquired:	5/25/2023 12:59:28 PM EDT		

Auto-Scaled Chromatogram
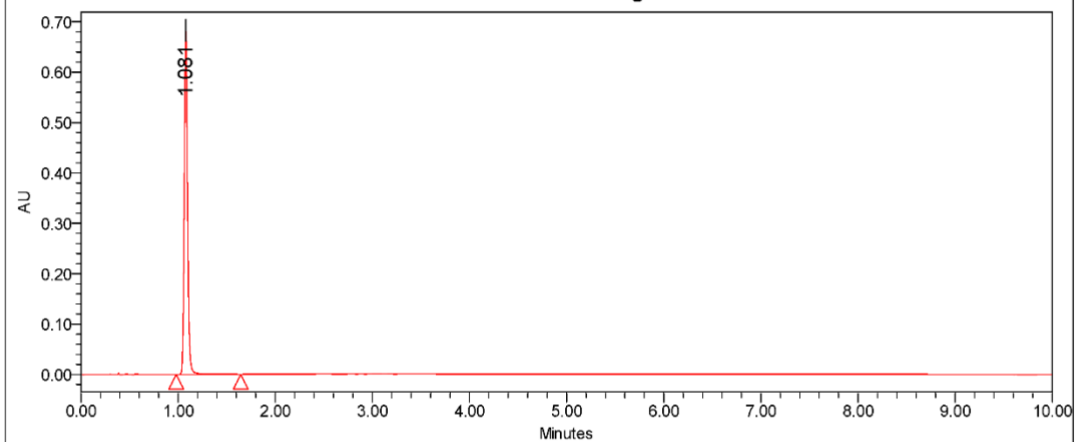
Peak Results

	RT	Area	Height	% Area
1	1.081	1637723	685415	100.00

Reported by User: System
Report Method: Default
Report Method ID: 23653
Page: 1 of 1

Date Printed:
3/21/2024
12:32:42 PM US/Eastern

1089

S A M P L E   I N F O R M A T I O N

Sample Name:	DQ
Sample Type:	Unknown
Vial:	1:A,6
Injection #:	1
Injection Volume:	1.00 ul
Run Time:	10.0 Minutes
Date Acquired:	5/25/2023 2:33:53 PM EDT

Acquired By:	System
Processing Method	10 min processing
Channel Name:	2998 Ch6 280nm@4.8nm
Proc. Chnl. Descr.:	2998 Ch6 280nm@4.8nm

Auto-Scaled Chromatogram
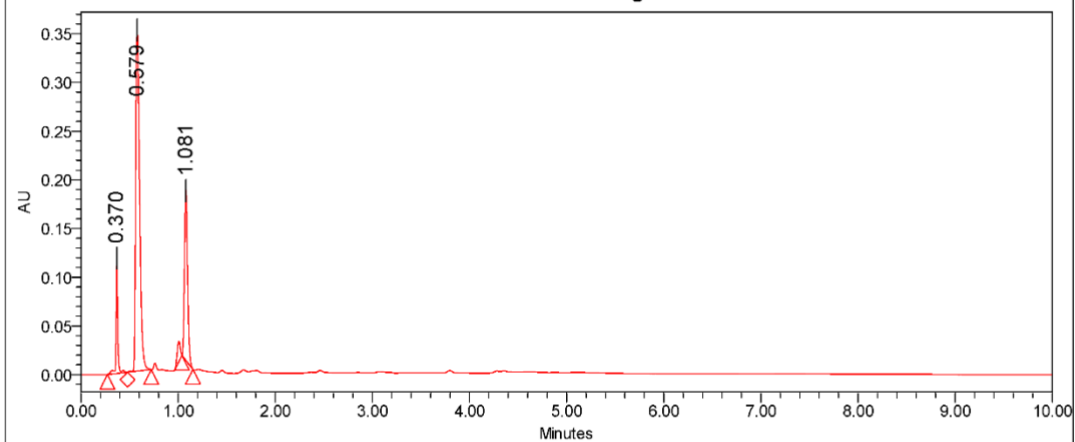
Peak Results

	RT	Area	Height	% Area
1	0.370	143723	118945	9.35
2	0.579	1001073	351106	65.15
3	1.081	391761	175183	25.50

Reported by User: System
Report Method: Default
Report Method ID: 23653
Page: 1 of 1

Date Printed:
3/22/2024
9:21:25 AM US/Eastern

1090

S A M P L E   I N F O R M A T I O N

Sample Name:	Exposed
Sample Type:	Unknown
Vial:	1:A,7
Injection #:	1
Injection Volume:	1.00 ul
Run Time:	10.0 Minutes
Date Acquired:	5/25/2023 1:23:16 PM EDT

Acquired By:	System
Processing Method	10 min processing
Channel Name:	2998 Ch6 280nm@4.8nm
Proc. Chnl. Descr.:	2998 Ch6 280nm@4.8nm

Auto-Scaled Chromatogram
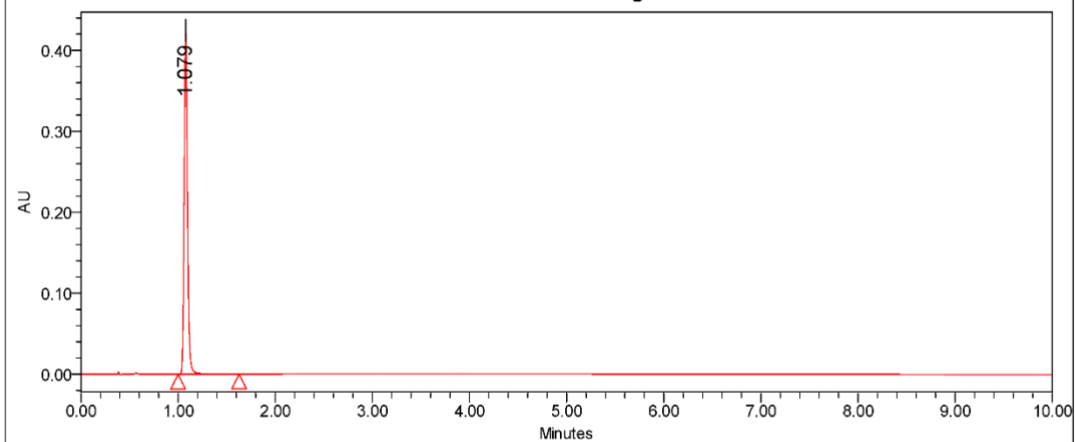
Peak Results

	RT	Area	Height	% Area
1	1.079	1035589	426262	100.00

Reported by User: System
Report Method: Default
Report Method ID: 23653
Page: 1 of 1

Date Printed:
3/21/2024
10:48:08 AM US/Eastern

1091

S A M P L E   I N F O R M A T I O N

Sample Name:	H2O Blank
Sample Type:	Unknown
Vial:	1:A,1
Injection #:	1
Injection Volume:	1.00 ul
Run Time:	10.0 Minutes
Date Acquired:	5/25/2023 12:47:35 PM EDT

Acquired By:	System
Processing Method	10 min processing
Channel Name:	2998 Ch6 280nm@4.8nm
Proc. Chnl. Descr.:	2998 Ch6 280nm@4.8nm

Auto-Scaled Chromatogram
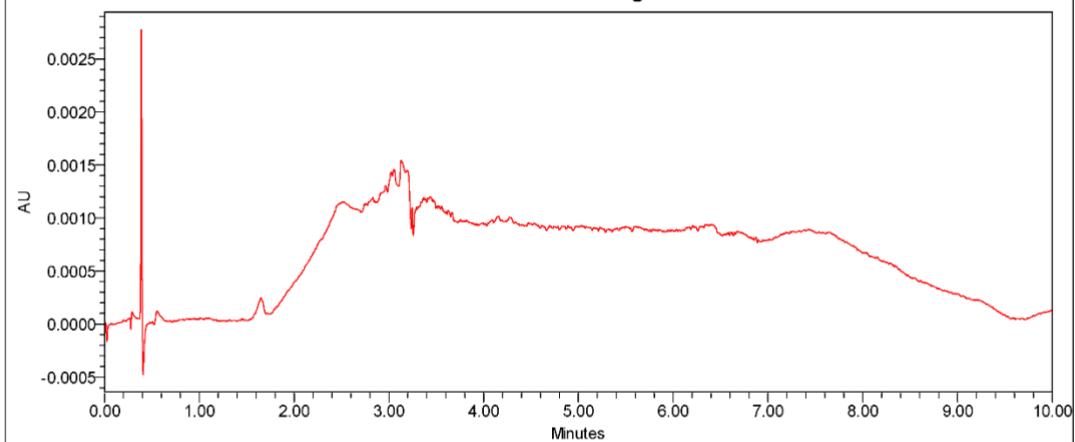
Peak Results

	RT	Area	Height	% Area
1				

Reported by User: System
Report Method: Default
Report Method ID: 23653
Page: 1 of 1

Date Printed:
3/21/2024
10:45:29 AM US/Eastern

1092

![hhmi | janelia Research Campus logo]

S A M P L E   I N F O R M A T I O N

Sample Name:	NaIO4	Acquired By:	System
Sample Type:	Unknown	Processing Method	10 min processing
Vial:	1:A,3	Channel Name:	2998 Ch6 280nm@4.8nm
Injection #:	1	Proc. Chnl. Descr.:	2998 Ch6 280nm@4.8nm
Injection Volume:	1.00 ul		
Run Time:	10.0 Minutes		
Date Acquired:	5/25/2023 1:47:03 PM EDT		

Auto-Scaled Chromatogram
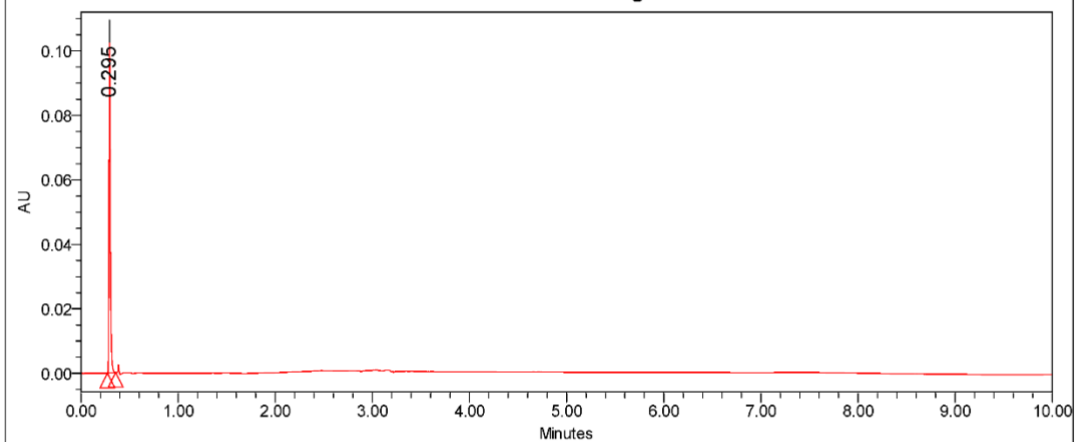
Peak Results

	RT	Area	Height	% Area
1	0.295	104084	106431	100.00

Reported by User: System
Report Method: Default
Report Method ID: 23653
Page: 1 of 1

Date Printed:
3/21/2024
12:35:46 PM US/Eastern

1093

43

hhmi | janelia
Research Campus

SAMPLE INFORMATION

Sample Name:	Unexposed
Sample Type:	Unknown
Vial:	1:A,8
Injection #:	1
Injection Volume:	1.00 ul
Run Time:	10.0 Minutes
Date Acquired:	5/25/2023 1:35:09 PM EDT

Acquired By:	System
Processing Method	10 min processing
Channel Name:	2998 Ch6 280nm@4.8nm
Proc. Chnl. Descr.:	2998 Ch6 280nm@4.8nm

Auto-Scaled Chromatogram
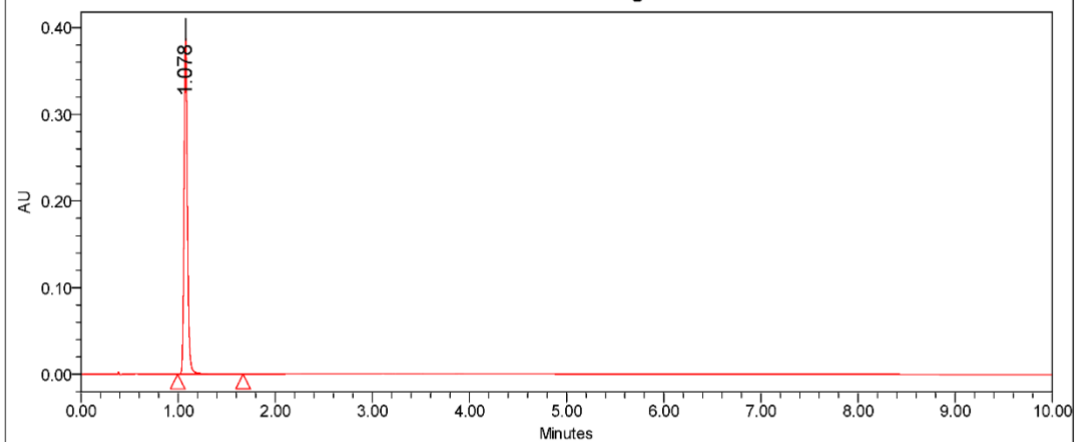
Peak Results

	RT	Area	Height	% Area
1	1.078	965002	397922	100.00

Reported by User: System
Report Method: Default
Report Method ID: 23653
Page: 1 of 1

Date Printed:
3/21/2024
10:48:29 AM US/Eastern

1094

1095

1096

44

Table S1. Normalized compound ΔF/F values used in study for Fig. 1b. Data arranged from high to low with DA
and OO bracketing as in Fig. 1.

Compound	ΔF/F (Norm., mean)	Standard Deviation	Compound	ΔF/F (Norm., mean)	Standard Deviation
DA	0.9330218069	0.05842679	K	0.0420560748	0.03738318
F	3.6651090343	0.11305450	W	0.0404984424	0.01641068
4	3.0809968847	0.37911953	U	0.0124610592	0.10294524
C	2.8037383178	0.16789948	WW	-0.0124610592	0.04416650
RR	2.7679127726	0.18493892	3	-0.0155763240	0.02573631
O	1.9252336449	0.08187577	6	-0.0389408100	0.00539580
MM	1.7398753894	0.05574932	J	-0.0436137072	0.01079159
UU	1.4890965732	0.15682659	DD	-0.0451713396	0.00269790
X	1.4672897196	0.53876296	S	-0.0498442368	0.03180775
KK	1.2788161994	0.05613963	CC	-0.0545171340	0.03805854
TT	1.0233644860	0.17440615	GG	-0.0560747664	0.02842412
2	0.8442367601	0.04996578	1	-0.0560747664	0.02472665
10	0.8348909657	0.22615728	ZZ	-0.0591900312	0.00539580
9	0.7367601246	0.03180775	8	-0.0623052960	0.01945482
D	0.5327102804	0.01401869	Q	-0.0638629283	0.01348949
7	0.5077881620	0.09137077	YY	-0.0669781931	0.01079159
EE	0.5062305296	0.01175987	P	-0.0669781931	0.02397945
Y	0.4968847352	0.07259302	FF	-0.0685358255	0.01641068
VV	0.4844236760	0.02573631	H	-0.0825545171	0.00539580
5	0.4766355140	0.01618739	M	-0.0887850467	0.02141391
SS	0.4485981308	0.03708997	G	-0.0887850467	0.00467290
LL	0.4221183801	0.08771282	PP	-0.0965732087	0.01348949
A	0.3504672897	0.03237478	JJ	-0.1261682243	0.00809370
I	0.3286604361	0.03974253	V	-0.1526479751	0.04214252
II	0.2757009346	0.03237478	Z	-0.1682242991	0.06491796
T	0.2087227414	0.03180775	BB	-0.1744548287	0.01888529
N	0.2087227414	0.02573631	AA	-0.2040498442	0.04240080
L	0.2087227414	0.11149863	XX	-0.2056074766	0.00809370
HH	0.1526479751	0.06098683	QQ	-0.2149532710	0.03527960
B	0.1355140187	0.04602270	E	-0.2881619938	0.02351973
R	0.0887850467	0.03649649	OO	-0.0996884735	0.00269790
NN	0.0420560748	0.03064224			

1100
1101

1102 **Table S2. ΔF/F and reduction potentials for Fig. 2b.** Data arranged from low to high as in figure.

1103

Compound ID from Yamabe et al. (Based on studies of Pelizzetti et al.)	Compound ID from this study	Compound Name	One electron oxidation (V)	ΔF/F (Norm., mean)	Standard Deviation
1	EE	3-methoxybenzene-1,2-diol	1.18	0.50623053	0.01175987
4	7	4(1,1-dimethylethyl) benzene-1,2-diol	1.20	0.50778816	0.09137077
5	T	benzene-1,2-diol	1.25	0.20872274	0.03180775
6	A	4-chlorobenzene-1,2-diol	1.25	0.35046729	0.03237478
7	9	(-)-4-[l-hydroxy-2(methylamino)ethyl]benzene-l,2-diol (Adrenaline)	1.28	0.73676012	0.03180775
9	U	2,3-dihydroxybenzoic acid	1.36	0.01246106	0.10294524
10	B	3,4-dihydroxybenzoic acid	1.38	0.13551402	0.04602270
12	K	3,4-dihydroxybenzonitrile	1.43	0.04205607	0.03738318
13	HH	4-nitrobenzene-1,2-diol	1.46	0.15264798	0.06098683

1104
1105

Table S3. ΔF/F and Hammett values for Fig. 2c. Data arranged from high to low as in figure.
1107

Entry No.	Compound ID and Substituent	σ	ΔF/F (Norm., mean)	Standard Deviation
1	F - R-NH$_2$	-0.570	3.66510903	0.11305450
2	C - R-OH	-0.325	2.80373832	0.16789948
3	KK - R-OMe	-0.331	1.27881620	0.05613963
4	DA - dopamine	-0.129	0.93302181	0.05842679
5	9 - norepinephrine	-0.028	0.73676012	0.03180775
6	D - R-Et	-0.170	0.53271028	0.01401869
7	7 - *t*-butyl	-0.144	0.50778816	0.09137077
8	EE - R-OMe	0.029	0.50623053	0.01175987
9	Y - R-CH$_3$	-0.148	0.49688474	0.07259302
10	LL - R-Cl	0.378	0.42211838	0.08771282
11	A - R-Cl	0.200	0.35046729	0.03237478
12	I - R-ketone	0.455	0.32866044	0.03974253
13	N - R-F	0.129	0.20872274	0.02573631
14	T - catechol	0.000	0.20872274	0.03180775
15	HH - R-NO$_2$	0.984	0.15264798	0.06098683
16	B - R-COOH-para	0.523	0.13551402	0.04602270
17	K - R-CN	0.618	0.04205607	0.03738318
18	U - R-COOH-meta	0.366	0.01246106	0.10294524

1108
1109

1110   **Table S4. Summary of simulations performed.**

1111

Analyte Type	Total Number of Atoms	Total Simulation Time (ns)
F	22255	6000
F$^+$	22324	6000
DA$^+$	22285	6000
C	22315	6000
C$^-$	22294	7000
Y	22306	6000
T	22303	6000
1	22315	6000
RR	22240	7000
YY$^+$	22216	7000

1112

1113

1114

1115